

Supercontinuum source directly from noise-like pulse emission in a Tm-doped all-fiber laser with nonlinear polarization rotation



A. Camarillo-Avilés^a, R. López-Estopier^{a,b}, O. Pottiez^c, M. Durán-Sánchez^{b,d}, B. Ibarra-Escamilla^d, M. Bello-Jiménez^{a,*}

^aInstituto de Investigación en Comunicación Óptica (IICO), Universidad Autónoma de San Luis Potosí, Av., Karakorum No. 1470 Lomas 4^a Secc., 78210 San Luis Potosí, Mexico

^bConsejo Nacional de Ciencia y Tecnología (CONACYT), Av. Insurgentes Sur No. 1582, Col. Crédito Constructor, Del. Benito Juárez, México 039040, D.F., Mexico

^cCentro de Investigaciones en Óptica (CIO), Loma del Bosque No. 115, Col. Lomas del Campestre, 37150 León, Guanajuato, Mexico

^dInstituto Nacional de Astrofísica, Óptica y Electrónica (INAOE), Luis Enrique Erro No 1, Departamento de Óptica, 72000 Puebla, Mexico

ARTICLE INFO

Keywords:

Fiber optic laser
Thulium-doped fiber
Noise-like pulse
Supercontinuum source
Nonlinear polarization rotation

ABSTRACT

Supercontinuum (SC) generation directly from noise-like pulse (NLP) emission is demonstrated in a mode-locked thulium-doped all-fiber laser with nonlinear polarization rotation. The laser supports NLP emission at a repetition rate of 812.79 kHz, producing optical pulses of 2 ns pulse duration and 400 nm of optical bandwidth, which expands from 1800 nm to 2200 nm at floor level and covers the entire thulium band. The SC source presents a high dynamic range, higher than 50 dB, a high degree of spectral flatness, without significant spectral variations or pump remnants, and an output average power of 20.25 mW. Moreover, our proposal avoids the inclusion of external components and devices, thus preserving the robustness and simplicity in a single all-fiber system.

1. Introduction

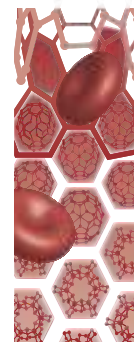
In recent years, fiber-optic light sources generating noise-like pulses (NLPs) have become essential optical sources with a great variety of applications in many research fields, such as spectral domain optical coherent tomography (You et al., 2015; Bizheva et al., 2003), nonlinear frequency conversion (Smirnov et al., 2014), optical metrology and sensing (Goloborodko et al., 2003; Putnam et al., 1998), micromachining (Mutlu Erdoğan et al., 2011; Özgören et al., 2011), low-coherence spectral interferometry (Keren et al., 2002, 2003; Keren and Horowitz, 2001), among others. One of the most distinguishing features of NLP sources is the emission of broad and smooth optical spectrum, exhibiting an optical bandwidth that is typically on the order of a few tens of nanometers (Liu et al., 2016, 2017; Michalska and Swiderski, 2019). In the time domain, NLP emission is also identified by nanosecond or sub-nanosecond bunches of pulses, comprising a pulse envelope that is composed of an inner structure of ultrashort optical sub-pulses with random peak amplitudes and distribution. These unique properties make NLP sources a very attractive solution to generate strong nonlinear phenomena in optical fibers. Their capacity of long-pulse generation is advantageous to avoid pulse dispersion over long distances, while maintaining high peak power

levels in their sub-pulse structure. Therefore, nonlinear effects are feasible in fibers with low nonlinear coefficients, such as conventional optical fibers, or in fibers whose dispersion is not especially designed for this purpose. In addition to these benefits, NLP emission does not seem to require a fine adjustment of the cavity parameters, and they can be found over a wide variety of fiber laser architectures, operation wavelengths and dispersion regimes. For a cavity operating through a nonlinear polarization rotation technique, polarization defines the nonlinear transmission of the passive mode locker. Therefore, it is common to access to a NLP regime by properly adjusting the pressure and orientation of the polarization controllers.

While there has been an exceptional progress in developing fiber-based NLP sources, the increasing demands for broader optical bandwidths have led researchers to investigate new schemes and alternatives to expand the NLP spectrum to reach a supercontinuum (SC) regime, where an issue of particular interest is the feasibility of NLPs to produce a large SC spectrum without the assistance of external fiber devices or components, such as double-clad power amplifiers or specialty nonlinear optical fibers. This added requirement can lead to the development of SC light sources based on a single fiber-optic system, making the SC source more robust, stable, with low economic cost and simple operation. Following this research line, only one

* Corresponding author.

E-mail address: miguel.bello@uaslp.mx (M. Bello-Jiménez).



TNF- α detection using gold nanoparticles as a surface-enhanced Raman spectroscopy substrate

Elizabeth Loredó-García¹, Alejandra Ortiz-Dosal², Juan Manuel Núñez-Leyva², José Luis Cuellar Camacho³, Jorge Alejandro Alegría-Torres⁴, Lizeth García-Torres⁵, Hugo Ricardo Navarro-Contreras¹ & Eleazar Samuel Kolosovas-Machuca^{*1}

¹Coordinación para la Innovación y Aplicación de la Ciencia y la Tecnología, Universidad Autónoma de San Luis Potosí. 550 Sierra Leona Ave., 78210 San Luis Potosí, SLP, México

²Doctorado Institucional en Ingeniería y Ciencia de Materiales (DICIM-UASLP), Universidad Autónoma de San Luis Potosí. 550 Sierra Leona Ave., 78210 San Luis Potosí, SLP, México

³Institute of Chemistry & Biochemistry, Freie Universität Berlin, Takustraße 3, 14195 Berlin, Germany

⁴Departamento de Farmacia, División de Ciencias Naturales y Exactas, Universidad de Guanajuato. Noria Alta s/n, 36050, Guanajuato, Gto., México

⁵Laboratorio de Investigación Molecular en Nutrición (LIMON), Universidad del Centro de México, UCEM, Capitán Caldera 75, 78250, San Luis Potosí, SLP, México

*Author for correspondence: samuel.kolosovas@uaslp.mx

Background: TNF- α is a cytokine involved in inflammation. Surface-enhanced Raman spectroscopy (SERS) could be useful in its detection. **Aim:** Identify the TNF- α in an aqueous solution, using gold nanoparticles (AuNPs) as a SERS substrate. **Materials & methods:** Raman and SERS spectra were obtained from TNF- α samples, combined with AuNPs, with decreasing concentrations of TNF- α . The samples were analyzed using optical transmission spectroscopy, dynamic light scattering, and transmission electron microscopy. **Results:** Transmission electron microscopy/dynamic light scattering determined a change in the average diameter of the TNF- α /AuNPs (\sim 9.6 nm). Raman bands obtained were associated with aromatic amino acid side chains. We observe Raman signals for TNF- α concentrations as low as 0.125 μ g/ml. **Conclusion:** TNF- α signal at physiological concentrations was determined with SERS.

First draft submitted: 30 July 2020; Accepted for publication: 5 November 2020; Published online: 24 December 2020

Keywords: biomarkers • cytokines • gold nanoparticles • SERS • TNF- α

Cytokines are a group of proteins and glycoproteins that act as regulators of immune and inflammatory responses. The cytokines group includes interleukins, TNFs, interferons, colony-stimulating factors and chemokines [1]. The TNF superfamily of cytokines engages specific cell surface receptors. These interactions activate signaling pathways for cell survival, apoptosis and differentiation that control immune function and disease [2]. TNF- α is a cytokine, constituted by 157 amino acids with a molecular weight of 17 kDa, which is well known to be involved in the genesis of inflammation and autoimmunity [3]. Activated macrophages and T cells synthesize this cytokine. Nevertheless, many other cells, such as B-cells, neutrophils and endothelial cells, have also been described to produce TNF- α during inflammation as TNF- α is directly related to protective immunity, cancer and autoimmunity. Its accurate quantification in the blood could assess cytokine response in different diseases [4]. When the immune system is working correctly, TNF- α acts beneficially to protect the organism. If tissue damage or infection occurs, TNF- α develops a pro-inflammatory action; this favors the recruitment of lymphocytes and neutrophils, as well as antigen recognition, which leads to remodeling and recovery of tissues [5,6,7]. Moreover, the concentration of TNF- α in the plasma of patients with cardiovascular diseases is higher than those found in healthy individuals. For instance, Ridker *et al.* have found that TNF- α plasma levels above 4.17 μ g/ml indicated an increased risk of recurrent coronary events, even after adjustment to conventional cardiovascular risk factors [8]. Indeed, the serum level of TNF- α has been reported approximately 100 μ g/ml in various hypertensive conditions in humans [9]. However,

Letter

Incipient mode locking dynamics in an all-normal dispersion ytterbium-doped fiber ring laser

J A Carrasco-Ramirez¹, O Pottiez¹, Y E Bracamontes-Rodriguez¹, J P Lauterio-Cruz^{1,2}, H E Ibarra-Villalon³, J C Hernandez-Garcia^{2,4} and M Bello-Jimenez⁵

¹ Centro de Investigaciones en Óptica A. C., Lomas del Bosque 115, Col. Lomas del Campestre, León, Gto, 37150, México

² Departamento de Electrónica, División de Ingenierías CIS, Universidad de Guanajuato, Carretera Salamanca-Valle de Santiago Km 3.5 + 1.8 Km, Comunidad de Palo Blanco, Salamanca, Gto, 36885, México

³ Departamento de Ciencias Básicas. Universidad Autónoma Metropolitana-Unidad Azcapotzalco, Av. San Pablo No. 180. Col. Reynosa Tamaulipas, Azcapotzalco, CDMX 02200, México

⁴ Consejo Nacional de Ciencia y Tecnología, Av. Insurgentes Sur No. 1582, Col. Crédito Constructor, Del. Benito Juárez, C.P. 039040, México

⁵ Instituto de investigación en Comunicación Óptica (IICO), Universidad Autónoma de San Luis Potosí, Av. Karakorum No. 1470 Lomas 4aSecc., 78210, San Luis Potosí, México

E-mail: pottiez@cio.mx

Received 21 July 2020

Accepted for publication 27 August 2020

Published 1 October 2020



Abstract

In this work we study experimentally the temporal dynamics of an all-normal dispersion all-fiber ring laser far from stable mode locking. Temporal mapping relying on segmented memory capabilities of a fast oscilloscope is used for this purpose. A regime is found where radiation fills the cavity and is characterized by peaks that successively emerge, grow in amplitude while compressing temporally, before decaying abruptly, and localized low-intensity components mediating their interactions across the cycles. The highest-amplitude peaks ephemerally dominate intracavity radiation, before being superseded by other emerging peaks. As radiation covers the whole period and no permanent pulse ever emerges, the regime can be viewed as an intermediate stage between continuous-wave and mode locking operations. The interest of using segmented memory possibilities for proper characterization of this unconventional regime is highlighted.

Keywords: mode-locked fiber lasers, laser dynamics, dissipative solitons

(Some figures may appear in color only in the online journal)

1. Introduction

Passively mode-locked fiber lasers are versatile sources of ultrashort pulses that are attractive for a broad range of applications. Although anomalous-dispersion sources were first studied for their ability to generate conservative solitons, it was later realized that, taking advantage of the interaction between

dispersive, nonlinear and dissipative effects, a broader variety of optical pulses could be tailored in normal-dispersion cavities [1–5], with energies often exceeding that of conventional solitons by several orders of magnitude. All-normal dispersion (ANDi) lasers are an example of such sources. Bandpass filtering is essential to guarantee stable dissipative soliton operation in such schemes, as it compensates the pulse

MAXIMUM RECTILINEAR CONVEX SUBSETS*

HERNÁN GONZÁLEZ-AGUILAR[†], DAVID ORDEN[‡], PABLO PÉREZ-LANTERO[§],
DAVID RAPPAPORT[¶], CARLOS SEARA^{||}, JAVIER TEJEL[#], AND JORGE URRUTIA^{††}

Abstract. Let P be a set of n points in the plane. We consider a variation of the classical Erdős–Szekeres problem, presenting efficient algorithms with $O(n^3)$ running time and $O(n^2)$ space complexity that compute (1) a subset S of P such that the boundary of the rectilinear convex hull of S has the maximum number of points from P , (2) a subset S of P such that the boundary of the rectilinear convex hull of S has the maximum number of points from P and its interior contains no element of P , (3) a subset S of P such that the rectilinear convex hull of S has maximum area and its interior contains no element of P , and (4) when each point of P is assigned a weight, positive or negative, a subset S of P that maximizes the total weight of the points in the rectilinear convex hull of S . We also revisit the problems of computing a maximum area orthoconvex polygon and computing a maximum area staircase polygon, amidst a point set in a rectangular domain. We obtain new and simpler algorithms to solve both problems with the same complexity as in the state of the art.

Key words. Erdős–Szekeres problems, convex subsets, optimization, rectilinear convex hull

AMS subject classification. 68U05

DOI. 10.1137/19M1303010

1. Introduction. Let P be a point set in general position in the plane. A subset S of P with k elements is called a *convex k -gon* if the elements of S are the vertices of a convex polygon, and it is called a *convex k -hole* of P if the interior of the convex hull of S contains no element of P . The study of convex k -gons and convex k -holes

*Received by the editors November 27, 2019; accepted for publication (in revised form) October 5, 2020; published electronically February 1, 2021. A preliminary version has been published at the 22nd International Symposium on Fundamentals of Computation Theory, FCT 2019, Springer, Cham, Switzerland, 2019, pp. 274–291. This version includes two new sections with applications, sections 5 and 6.

<https://doi.org/10.1137/19M1303010>

Funding: This work has received funding from the European Union’s Horizon 2020 research and innovation programme under the Marie Skłodowska-Curie grant agreement 734922. The second author was supported by projects MTM2017-83750-P of the Spanish Ministry of Science (AEI/FEDER, UE) and PID2019-104129GB-I00 / AEI / 10.13039/501100011033 of the Spanish Ministry of Science and Innovation. The third author was partially supported by projects DI-CYT 041933PL Vicerrectoría de Investigación, Desarrollo e Innovación USACH (Chile), and Programa Regional STICAMSUD 19-STIC-02. The fifth author was supported by projects MTM2015-63791-R MINECO/FEDER, Gen. Cat. DGR 2017SGR1640, and PID2019-104129GB-I00 / AEI / 10.13039/501100011033 of the Spanish Ministry of Science and Innovation. The sixth author was supported by projects MTM2015-63791-R MINECO/FEDER, Gobierno de Aragón E41-17R, and PID2019-104129GB-I00 / AEI / 10.13039/501100011033 of the Spanish Ministry of Science and Innovation. The seventh author was supported by PAPIIT grant IN102117 from UNAM.

[†]Facultad de Ciencias, Universidad Autónoma de San Luis Potosí, México (hernan@fc.uaslp.mx).

[‡]Departamento de Física y Matemáticas, Universidad de Alcalá, Alcalá de Henares, Madrid, 28871, Spain (david.orden@uah.es).

[§]Departamento de Matemática y Ciencia de la Computación, USACH, Santiago de Chile, Chile (pablo.perez.l@usach.cl).

[¶]School of Computing, Queen’s University, Kingston, Canada (daver@cs.queensu.ca).

^{||}Departament de Matemàtiques, Universitat Politècnica de Catalunya, Barcelona, Spain (carlos.seara@upc.edu).

[#]Departamento de Métodos Estadísticos, IUMA, Universidad de Zaragoza, Zaragoza, 50009, Spain (jtejel@unizar.es).

^{††}Instituto de Matemáticas, Universidad Nacional Autónoma de México, Coyoacán, México, D. F., 04510 (urrutia@matem.unam.mx).

**RESEARCH ARTICLE**

Structural and Raman study of the thermoelectric solid solution $\text{Sr}_{1.9}\text{La}_{0.1}\text{Nb}_2\text{O}_7$

Hiram Joazet Ojeda-Galván^{1,2} | Ma. del Carmen Rodríguez-Aranda¹ |
Ángel Gabriel Rodríguez¹ | Javier Alanis^{1,3} | Jorge Íñiguez^{5,6} |
María Eugenia Mendoza⁴ | Hugo Ricardo Navarro-Contreras¹

¹Coordination for the Innovation and Application of Science and Technology (CIACYT), Autonomous University of San Luis Potosí, San Luis Potosí, 78000, Mexico

²Center for Research in Health Sciences and Biomedicine (CICSAB), Autonomous University of San Luis Potosí, San Luis Potosí, 78000, Mexico

³Science Faculty, Autonomous University of San Luis Potosí, San Luis Potosí, 78000, Mexico

⁴Institute of Physics, Luis Rivera Terrazas, Meritorious Autonomous University of Puebla, Puebla, 72570, Mexico

⁵Materials Research and Technology Department, Luxembourg Institute of Science and Technology (LIST), Esch-sur-Alzette, L-4362, Luxembourg

⁶Physics and Materials Research Unit, University of Luxembourg, Belvaux, L-4422, Luxembourg

Correspondence

Javier Alanis and Hugo R. Navarro-Contreras, Coordination for the Innovation and Application of Science and Technology (CIACYT), Autonomous University of San Luis Potosí, Álvaro Obregón 64, San Luis Potosí, S.L.P. 78000, Mexico.
Email: javier.alanis.perez@hotmail.com; hnavarro@uaslp.mx

Funding information

Consejo Nacional de Ciencia y Tecnología, Grant/Award Numbers: Ciencia Básica 256788, Estancias Posdoctorales 2018(1), Problemas Nacionales 2015-01-986; Secretaría de Educación Pública: Estancias Posdoctorales PRODEP 2019; Fonds National de la Recherche Luxembourg, Grant/Award Number: FNR/P12/4853155

Abstract

Ceramic powder samples of the perovskite-slab-layered polycrystalline $\text{Sr}_{1.9}\text{La}_{0.1}\text{Nb}_2\text{O}_7$ (SLNO1) thermoelectric solid solution were prepared via solid-state reaction. The Raman effect was studied as a function of temperature between 27°C and 400°C (at ambient pressure) and pressures up to 11.6 GPa (at room temperature). The atomic disorder introduced by the La atoms produced phonon lines that were broader than those of $\text{Sr}_2\text{Nb}_2\text{O}_7$ (SNO). We detected a temperature-induced phase transition at $T_{i-c} = 247 \pm 5^\circ\text{C}$ (ambient pressure) and a pressure-induced phase transition at $P_{i-c} = 6.74 \pm 0.25$ GPa (room temperature), which correspond to the reported SNO incommensurate-to-commensurate phase transitions at 215°C (atmospheric pressure) and $P_{i-c} = 6.54 \pm 0.25$ GPa (27°C), respectively. In this paper, the phenomenological and structural differences between SNO and SLNO1 are discussed based on density functional theory calculations of $\text{Sr}_{2-x}\text{La}_x\text{Nb}_2\text{O}_7$ ($x = 0.0625$ and 0.125) supercells.

KEYWORDS

DFT, Grüneisen parameters, high pressure, layered perovskite, phase transition

RESEARCH ARTICLE

Frustules of *Amphora* sp. as a photonic crystal with photoluminescent CdS nanoparticles

Georgina González-Fortuna¹ | Nubia Arteaga-Larios¹ | Yuri Nahmad² |
Hugo R. Navarro-Contreras³ | J. Viridiana García-Meza¹ 

¹Geomicrobiology Laboratory, Metallurgy, UASLP, Sierra Leona 550, 78210 SLP, Mexico

²Institute of Physics, UASLP, Dr. Manuel Nava 8, 78217, SLP, Mexico

³CIACyT, Center for the Innovation and Application of Science and Technology, UASLP, Sierra Leona 550, 78210 SLP, Mexico

Correspondence

J. Viridiana García-Meza, Geomicrobiology Laboratory, Metallurgy, UASLP, Sierra Leona 550, 78210 SLP, Mexico.
Email: jvgm@uaslp.mx

Abstract

Diatom frustules have species-specific patterns of pores, striae, pores, and nanopores, periodically arranged on its silica surface, as sets of cavities that modify the vacuum electromagnetic density of states. Therefore, frustules may be considered photonic crystals; the interaction with light-emitting sources inside the pores may potentially result in enhancement or inhibition of their spontaneous radiative emission rate and frequencies. In this work, we studied the photoluminescence of cadmium sulfide nanoparticles (CdS-NP) deposited inside frustule cavities that conveyed evidence of cavity-NP interaction. We synthesized CdS-NP, a semiconductor compound achieving quantum dots small enough to impose confinement effects to the electronic states. CdS-NP and their clusters were physisorbed onto the surface, striae, and predominantly inside the pores of the cleansed frustules of *Amphora* sp. A broad peak with a maximum intensity at 437 nm (2.84 eV) was recorded after excitation with a 375 nm light source, showing a large blue shift and signal amplification of the CdS-NP photoluminescence when these were embedded inside the pores of the silica frustule. Using the Brus equation, we estimated a NP size of 4.1 ± 0.2 nm for the CdS-NP snugly packed inside the smaller pores of the frustule, of 10 ± 0.7 nm in average diameter. The emission Purcell enhancement factor for an emitting atom in a cavity was calculated. The obtained Q factor (c. 5) was smaller than typical Q factors for designed semiconductor cavities of similar dimensions, an expected situation if it is assumed that the pores are open-ended cavities.

KEYWORDS

Amphora sp, optical cavities, photoluminescence, photonic crystal, Purcell effect

1 | INTRODUCTION

Diatoms are photosynthetic, unicellular microorganisms whose main characteristic is that they assimilate silicic acid dissolved in water and incorporate it into their cell wall in the form of amorphous silica (SiO₂) or biosilica named frustule. Diatom frustules have species-specific patterns of pores hierarchically arranged at the micrometre to nanometre scale that display efficient luminescence. Geometrically speaking, their distribution and diversity make diatoms individually

unique, 'they are the snowflakes of (the liquid state of) water and they are evolutionarily very stable solutions'.^[1] Specifically, the structure of the frustule imparts the ability to focus light as an antenna or antenna arrays, to manipulate light for optimal use during photosynthesis avoiding photoinhibition and protect living diatoms from DNA detrimental ultraviolet (UV) radiation.^[1-3]

However, this novel light-focusing ability conferred by the frustule and their ornaments, requires an increase in oily products to compensate for the buoyancy lost due to the high density of the frustule.

Multiple mode-locked regimes of an Er/Yb double-clad fiber laser based on NPR

Manuel Durán-Sánchez^{1,2,*}, Olivier Pottiez³ , Berenice Posada-Ramírez¹ , Ricardo I Álvarez-Tamayo⁴ , Iván Armas-Rivera¹, Miguel Bello-Jiménez⁵, Yasser A García-Flores¹, E Montiel-Piña⁶ and Baldemar Ibarra-Escamilla¹

¹ Instituto Nacional de Astrofísica, Óptica y Electrónica, Luis Enrique Erro, Sta. María Tonantzintla, Puebla 72824, Mexico

² CONACyT—Instituto Nacional de Astrofísica, Óptica y Electrónica, Luis Enrique Erro, Sta. María Tonantzintla, Puebla 72824, Mexico

³ Centro de Investigaciones en Óptica A. C., Lomas del Bosque 115, Col. Lomas Campestre, León, Gto. 37150, Mexico

⁴ Universidad Popular Autónoma del Estado de Puebla, 17 Sur 901 Col. Santiago, Puebla 72160, México

⁵ Instituto de Investigación en Comunicación Óptica, Universidad Autónoma de San Luis Potosí, Av. Karakorum, San Luis Potosí, S. L.P. 78210, México

⁶ Facultad de Ingeniería de la Universidad Autónoma de Puebla, Apartado postal J39, 72570 Puebla, Pue., México

E-mail: manueld@inaoep.mx

Received 2 September 2020, revised 22 February 2021

Accepted for publication 10 March 2021

Published 26 March 2021



CrossMark

Abstract

In this paper, we experimentally demonstrate generation of diverse structures of robust optical pulses obtained with a ring cavity passively mode-locked fiber laser based on a double-clad erbium-ytterbium doped fiber, and operating at net-anomalous cavity dispersion. A half-wave and a quarter-wave retarder plates allow adjustable saturable absorbing action by the nonlinear polarization rotation technique. Pulsed laser operation in quasi-continuous wave, molecules of solitons, and single-wavelength noise-like pulses (NLPs) regimes is obtained by properly adjusting the wave retarders. In the soliton and NLPs operating regimes, the central laser wavelength lies in the 1540 nm region. The obtained NLPs exhibit narrow peak coherence of ~ 231 fs.

Keywords: fiber lasers, mode-locked lasers, pulse propagation, temporal solitons

(Some figures may appear in colour only in the online journal)

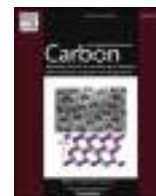
1. Introduction

During the last decade, mode-locked (ML) lasers have been attracting attention for their development in fiber-based cavities [1, 2]. Fiber laser technology meets the demands and requirements for a wide range of applications due to the advantages of fiber systems such as compactness, high-quality

beam generation, relatively low cost and capacity to produce ultra-short optical pulses with high peak powers and repetition rates. In the framework of photonic applications, pulses of ultra-short duration have become essential in many research areas such as fiber communications, optical instrumentation, and particularly in nonlinear optics for THz wave generation, comb generation, soliton generation [3–6] and many others.

Passively ML (PML) fiber lasers can operate in single-, dual- [7–9] or even multi-wavelength [10] emission. When ML single- or dual-wavelength laser emission is achieved,

* Author to whom any correspondence should be addressed.



Research Article

Myeloperoxidase-induced degradation of N-doped carbon nanotubes: Revealing possible atomistic mechanisms underlying hypochlorite-driven damage of nanotube walls



G. Azuara-Tuexi ^a, J.A. Méndez-Cabañas ^a, E. Muñoz-Sandoval ^b, R.A. Guirado-López ^{a,*}

^a Instituto de Física “Manuel Sandoval Vallarta”, Universidad Autónoma de San Luis Potosí, Álvaro Obregón 64, San Luis Potosí, SLP, 78000, Mexico

^b Advanced Materials Division, IPICYT, Camino a La Presa, San José 2055, San Luis Potosí, SLP, 78216, Mexico

ARTICLE INFO

Article history:

Received 14 October 2020

Received in revised form

12 January 2021

Accepted 15 January 2021

Available online 17 January 2021

Keywords:

Carbon nanotubes

Density functional theory

Raman spectroscopy

Enzymatic

Degradation

Thermogravimetric analysis

Transmission electron microscopy

ABSTRACT

We present a combined experimental and theoretical study dedicated to analyze the human myeloperoxidase (h-MPO)-catalyzed degradation of oxidized nitrogen-doped multi-walled carbon nanotubes (NMWCNTs-Ox) in vitro at 27 °C. NMWCNTs are synthesized by the aerosol assisted chemical vapor deposition (AACVD) technique and are characterized by employing transmission electron microscopy (TEM), scanning electron microscopy (SEM), thermal gravimetric analysis (TGA), as well as Raman and X-ray photoelectron spectroscopies. H-MPO degradation, involving hypochlorous acid and hypochlorite species, leads to complete removal of CNTs with diameters smaller than 75 nm from the samples. Simultaneously, for larger sizes, it produces the formation of highly deformed NMWCNTs decorated with NaCl nanoparticles, which exhibit reduced cytotoxicity in exposed monocytes studies compared with the initial nanotube samples. Density functional theory (DFT) calculations performed on model nitrogen-doped CNTs are also presented to explore, at an atomistic level, the fundamental aspects underlying degradation. Our DFT results reveal that reactivity of carbon walls is significantly affected around N-doped pyridinic, pyrrolic, and substitutional sites, leading to the existence of HClO molecules physisorbed close to those defects and high local concentrations of chemisorbed ClO species on C atoms adjacent to the N-rich regions. The formation of these hypochlorite molecular islands on the nanotube surface facilitates ClO dissociation producing strongly bound O species and Cl atoms that can be carbon bonded or released into the environment. The previous surface reaction results in the cleavage of the underlying C–C bonds, creating holey regions on the graphitic walls. The continuation of this process would lead to the formation of larger holes on the nanotube surface, allowing, on the one hand, the permeation of ClO molecules to the internal layers and, on the other hand, producing a reduction of the NMWCNTs diameter as observed from our experimental data.

© 2021 Published by Elsevier Ltd.

1. Introduction

The importance of using carbon nanotubes for medical applications has been established since years ago [1]. However, few studies have addressed the elimination of CNTs after fulfilling their assignment as therapeutic agents. Recently, Allen and collaborators studied a biodegradation mechanism of single-wall carbon nanotubes by horseradish peroxidase [2–4]. Alternatively, Kagan et al. degraded carbon nanotubes using neutrophil myeloperoxidase and demonstrated such nanomaterials were less toxic [4–6]. Vlasova

et al. proposed that the myeloperoxidase-induced biodegradation of CNT is through hypochlorite action [6]. Both oxidized single-walled and multi-walled CNTs and nitrogen-doped bamboo-like structures have been degraded, and the role played by the i) incubation time [3,4,7], ii) nanotube's diameter [5,8], iii) degree of functionalization [7–9], and iv) concentration of sidewall defects [10,11] has been underlined. In particular, h-MPO-driven degradation is essential to emphasize since both oxidized and nitrogenated carbon nanotubes have the potential to be used in biomedicine for diagnostic applications [12] and as effective delivery vehicles [13,14] for a wide variety of biomolecules and drugs. Consequently, not only their toxicity but also their complete removal from the human body becomes essential.

* Corresponding author.

E-mail address: guirado@ifisica.uaslp.mx (R.A. Guirado-López).



OPEN

Ratio-based multi-level resistive memory cells

Miguel Angel Lastras-Montaña¹✉, Osvaldo Del Pozo-Zamudio¹, Lev Glebsky¹, Meiran Zhao², Huaqiang Wu² & Kwang-Ting Cheng³✉

Ratio-based encoding has recently been proposed for single-level resistive memory cells, in which the resistance ratio of a pair of resistance-switching devices, rather than the resistance of a single device (i.e. resistance-based encoding), is used for encoding single-bit information, which significantly reduces the bit error probability. Generalizing this concept for multi-level cells, we propose a ratio-based information encoding mechanism and demonstrate its advantages over the resistance-based encoding for designing multi-level memory systems. We derive a closed-form expression for the bit error probability of ratio-based and resistance-based encodings as a function of the number of levels of the memory cell, the variance of the distribution of the resistive states, and the ON/OFF ratio of the resistive device, from which we prove that for a multi-level memory system using resistance-based encoding with bit error probability x , its corresponding bit error probability using ratio-based encoding will be reduced to x^2 at the best case and $x^{\sqrt{2}}$ at the worst case. We experimentally validated these findings on multiple resistance-switching devices and show that, compared to the resistance-based encoding on the same resistive devices, our approach achieves up to 3 orders of magnitude lower bit error probability, or alternatively it could reduce the cell's programming time and programming energy by up 5–10x, while achieving the same bit error probability.

Resistive random-access memory (ReRAM) is a promising non-volatile memory technology for the next generation of high-performance and large capacity memories¹. A ReRAM device encodes information by modulating the electrical resistance of a thin oxide layer that is sandwiched between two electrodes. The physical resistance-switching mechanism in ReRAM devices have been described by the partial formation and destruction of a conductive filament (CF) in the oxide layer^{2–4}, and multiple resistance levels have been experimentally observed^{5–9}, which opens up the possibility of multi-level cells (MLC) as well as analog-based computing^{9–14}.

A major hurdle of this technology has been the large device-to-device and cycle-to-cycle variations^{7,9,15}, that are due to the intrinsic stochasticity in the formation and destruction of the CF¹⁶. Such variations manifest in a large resistance distribution of the memory states, which is particularly problematic for MLC memories that require tight state distributions to reliably pack as many levels as possible into a memory cell. Extensive efforts have been made to address ReRAM device variations through multiple approaches, spanning from device and circuit improvements^{17–21}, the use of a current compliance during the formation and destruction of the CF^{22–24}, to higher level write-verify programming schemes based on iterative algorithms to achieve high-precision state tuning^{6,7,9,25}.

To address the variability of MLC ReRAM devices, our proposal generalizes the idea in²⁶ which uses the *ratio of two devices' resistances*, rather than one device's absolute resistance (Fig. 1a), to encode information. Specifically, we use two serially-connected resistance-switching devices configured as a voltage divider (Fig. 1b). The state of the memory cell is determined by applying a non-destructive read voltage V_{read} across the voltage divider and comparing the voltage at the mid-point (V_{state}) to a reference voltage V_{ref} . The proposed solution is orthogonal to the mentioned device and circuit solutions, and in fact it greatly benefits from any improvements due to these sources.

To illustrate the potential of our ratio-based encoding (RatioBE) against the traditional resistance-based encoding (ReBE) in terms of the bit error probability (BEP), we first use a two-level resistance-switching device. Assume that the lowest (R_{on}) and highest (R_{off}) resistance states of the device are log-normally distributed and centered in 1 k Ω (logic '1') and 100 k Ω (logic '0'), respectively (Fig. 1c). Further defining a resistance reference R_{ref} , we estimate the BEP by deriving the probabilities $\text{Pr}(R_{\text{on}} > R_{\text{ref}})$ and $\text{Pr}(R_{\text{off}} < R_{\text{ref}})$. Figure 1d shows with dashed lines such probabilities and with a solid line their sum, as a function of R_{ref} . The variances of the R_{on} and

¹Instituto de Investigación en Comunicación Óptica, Facultad de Ciencias, Universidad Autónoma de San Luis Potosí, San Luis Potosí, México. ²Institute of Microelectronics, Tsinghua University, Beijing, China. ³School of Engineering, Hong Kong University of Science and Technology, Clear Water Bay, Kowloon, Hong Kong. ✉email: miguel.lastras@uaslp.mx; timcheng@ust.hk

A novel disposable sensor for measure intra-abdominal pressure

Nuevo sensor desechable para medir la presión intraabdominal

José S. Camacho-Juárez^{1*}, Bersaín Alexander-Reyes¹, Antonio Morante-Lezama¹,
Martín Méndez-García¹, Hernán González-Aguilar¹, Ildelfonso Rodríguez-Leyva², Oscar F. Nuñez-Olvera³,
Carlos Polanco-González⁴, Luis A. Gorordo-Delso⁴ y Jorge A. Castañón-González^{4,5}

¹Facultad de Ciencias, Universidad Autónoma de San Luis Potosí, San Luis Potosí; ²Facultad de Medicina, Universidad Autónoma de San Luis Potosí, San Luis Potosí; ³Instituto de Investigación en Comunicación Óptica, Universidad Autónoma de San Luis Potosí, San Luis Potosí; ⁴Facultad de Ciencias, Universidad Autónoma de México, Ciudad de México; ⁵Unidad de Cuidados Intensivos, Hospital Juárez de México, Ciudad de México. México

Abstract

Background: Measurement of intra-abdominal pressure (IAP) is realized with the Kron's method. However, this technique has drawbacks like an infusion of water into the bladder of the patient. **Objective:** The prove a new novel disposable sensor in the way to measure the IAP (DSIAP) this one addresses some limitations of the Kron method. **Materials and methods:** The DSIAP was tested in vitro and clinical settings. The proposed technique was compared with Kron's method through Pearson correlation and Bland-Altman analysis. For in vitro tests, 159 measurements were taken performed by simulating the IAP in the bladder. For the clinical test, 20 pairs of measurements were made in patients with routine IAP monitoring in the intensive care unit. **Results:** In vitro measurements showed a strong correlation between the DSIAP and the reference ($r = 0.99$, p -value $< 2.2 \times 10^{-16}$). The bias and 95% confidence intervals were 0.135 and -0.821 - 1.091 cm H₂O, respectively. Measurements in patients with DSIAP versus Kron's method shown a very good correlation ($r = 0.973$, p -value $< 5.46 \times 10^{-13}$), while the bias and confidence intervals were 0.018 and -3.461 - 3.496 mmHg, respectively. **Conclusions:** The results suggest that the proposed DSIAP showed a profile similar to pressure transducers already in clinical use while overcoming some limitations of the former.

Key Words: Disposable sensor. Intra-abdominal pressure. Pressure transducer. Kron's method.

Resumen

Antecedentes: La medición de la presión intraabdominal (PIA) generalmente se realiza con el método de Kron, a pesar de presentar inconvenientes como la infusión de agua en la vejiga del paciente. **Objetivo:** Introducir un nuevo sensor desechable para medir la PIA (SDPIA) que aborda algunas limitaciones del método de Kron. **Método:** Se probó el SDPIA en pruebas in vitro y clínicas. La técnica se contrastó con el método de Kron empleando la correlación de Pearson y el análisis de Bland-Altman. Para las pruebas in vitro se realizaron 159 mediciones simulando la PIA en la vejiga. Para las pruebas clínicas se realizaron 20 mediciones en pacientes con monitorización rutinaria de la PIA en la unidad de cuidados intensivos. **Resultados:** En las mediciones in vitro se encontró una alta correlación ($r = 0.99$; $p < 2.2 \times 10^{-16}$). El sesgo para la diferencia entre los dos métodos de medición fue de 0.135 cm H₂O, con un intervalo de confianza del 95% de -0.821 a 1.091 cm H₂O. En las mediciones clínicas también se encontró una

Correspondencia:

*José S. Camacho-Juárez

Facultad de Ciencias

Avda. Parque Chapultepec, 1570

C.P. 78210, San Luis Potosí, S.L.P., México

E-mail: sergio_camacho@fc.uaslp.mx

Fecha de recepción: 20-09-2018

Fecha de aceptación: 26-06-2019

DOI: 10.24875/CIRU.19000756

Cir Cir. 2020;88(1):7-14

Contents available at PubMed

www.cirurgiaycirujanos.com

0009-7411/© 2019 Academia Mexicana de Cirugía. Publicado por Permanyer. Éste es un artículo open access bajo la licencia CC BY-NC-ND (<http://creativecommons.org/licenses/by-nc-nd/4.0/>).

Switchable dissipative soliton resonance and noise like pulses regimes in a mode-locked double-clad thulium doped fiber laser

M Durán-Sánchez^{1,2}, B Posada-Ramírez¹, R I Álvarez-Tamayo³, M Bello-Jiménez⁴, Y A García-Flores¹, I Armas-Rivera¹, E Montiel-Piña⁵, E A Kuzin¹ and B Ibarra-Escamilla¹

¹ Instituto Nacional de Astrofísica, Óptica y Electrónica, Luis Enrique Erro, Sta. María Tonantzintla, Puebla 72824, Mexico

² CONACyT—Instituto Nacional de Astrofísica, Óptica y Electrónica, Luis Enrique Erro, Sta. María Tonantzintla, Puebla 72824, Mexico

³ Universidad Popular Autónoma del Estado de Puebla, 17 Sur 901 Col. Santiago, Puebla 72160, México

⁴ Instituto de Investigación en Comunicación Óptica, Universidad Autónoma de San Luis Potosí, Av. Karakorum, S.L.P. 78210, México

⁵ Facultad de Ingeniería de la Universidad Autónoma de Puebla, Apartado postal J39, Puebla, Pue 72570, México

E-mail: manueld@inaoep.mx

Received 20 August 2020

Accepted for publication 14 December 2020

Published 30 December 2020



Abstract

We report an experimental study of switchable rectangular pulses generation in a passively mode-locked double-clad thulium-doped fiber laser operating in the anomalous dispersion regime. A fiber loop mirror and a polarization imbalanced nonlinear optical loop mirror (NOLM) forms the linear cavity. The loop in the NOLM includes a quarter-wave retarder, which allows switching between two regimes of rectangular pulse generation. The laser generates rectangular noise-like pulses (NLPs) or dissipative soliton resonance (DSR) pulses with 1.18 MHz repetition rate at ~ 1990 nm. At the maximum pump power of 10 W, rectangular pulses with energy of up to 540 nJ in DSR operation and 482 nJ in NLP operation were obtained with output average power of 640 mW and 571 mW, respectively.

Keywords: lasers, fiber, mode-locked lasers, pulse propagation, temporal solitons

(Some figures may appear in colour only in the online journal)

1. Introduction

During the last decade, passively mode-locked fiber lasers (PMLFLs) are of persistent interest due to their applications in different areas such as remote sensing [1], material processing [2], medical applications [3], generation of mid-infrared supercontinuum [4], among others. Typically, nonlinear absorption of different materials including graphene [5], carbon nanotubes [6], semiconductor saturable absorber mirror [7] has been used in order to include a saturable absorber

element within the laser cavity in order to generate passive mode locking laser pulses. In recent years, artificial saturable absorbers based on the nonlinear polarization evolution (NPE) phenomenon [8] or the use of a nonlinear optical loop mirror (NOLM) [9] stand for a reliable option for passively mode-locked laser emission. PMLFLs are able to generate different pulse regimes including stationary solitons, coupled solitons, solitons molecules, among others [10]. From the variety of different pulse shapes, those of noise-like pulses (NLPs) and dissipative soliton resonance (DSR) are of special interest due to

Letter

Tunable synchronized dual-wavelength pulsed operation in an Er/Yb double-clad fiber laser

M Durán-Sánchez^{1,2,*}, R I Álvarez-Tamayo³, Y A García-Flores¹, O Pottiez⁴, B Posada-Ramírez¹, M Bello-Jiménez⁵, J Alaniz-Balón¹, I Armas-Rivera¹, E Montiel-Piña⁶ and B Ibarra-Escamilla¹

¹ Instituto Nacional de Astrofísica, Óptica y Electrónica, Luis Enrique Erro 1, Santa María Tonantzintla, Puebla 72824, Mexico

² CONACyT—Instituto Nacional de Astrofísica, Óptica y Electrónica, Luis Enrique Erro 1, Santa María Tonantzintla, Puebla 72824, Mexico

³ Universidad Popular Autónoma del Estado de Puebla, 17 Sur 901 Col. Santiago, Puebla, Puebla 72410, México

⁴ Centro de Investigaciones en Óptica, A.C., Loma de Bosque 115, Col. Lomas del Campestre, León, Guanajuato 37115, México

⁵ Instituto de Investigación en Comunicación Óptica, Universidad Autónoma de San Luis Potosí, Av. Karakorum, San Luis Potosí, San Luis Potosí 78210, México

⁶ Facultad de Ingeniería, Benemérita Universidad Autónoma de Puebla, Apartado Postal J39, Puebla, Puebla 72570, México

E-mail: manueld@inaoep.mx

Received 18 January 2021

Accepted for publication 2 April 2021

Published 20 April 2021



CrossMark

Abstract

We present a simple and efficient experimental approach to synchronized dual-wavelength pulsed operation in an all-fiber laser. Four different dual-wavelength emissions of synchronized picosecond pulses are generated through simple adjustments of a wave retarder. Autocorrelation traces exhibit modulation profiles corresponding to dual-wavelength emissions with wavelength separations ranging over one order of magnitude, from 0.96 to 9 nm. In all cases, it is observed stable dual-wavelength operation and perfect synchronization between both pulsed components, without requiring of intra-cavity dispersion management. For the first time, to the best of our knowledge, synchronous tunable dual-wavelength pulse emission in a single-cavity Er/Yb double clad ring fiber laser is experimentally demonstrated.

Keywords: fiber laser, multiple solitons, dual-wavelength

(Some figures may appear in colour only in the online journal)

1. Introduction

During the last decades, dual-wavelength fiber lasers (DWFLs) have attracted attention for a wide range of potential

applications due to the versatility of fiber-based configurations in order to obtain multi-wavelength simultaneous laser generation. Application areas of DWFLs include optical fiber sensing, wavelength division multiplexing (WDM) and time division multiplexing (TDM) fiber communications, optical instrumentation, biomedical research, THz generation, laser comb and soliton generation, infrared spectroscopy and many

* Author to whom any correspondence should be addressed.

Phase and amplitude reconstruction in single-pixel transmission microscopy: A comparison of Hadamard, cosine, and noiselet bases

A. SANTOS-AMADOR,^{1,4} M. ARAIZA-ESQUIVEL,^{2,*} H. GONZÁLEZ,^{2,3} A. RODRÍGUEZ-COBOS,¹ E. TAJAHUERCE,³ L. MARTÍNEZ LEÓN,³ G. RAMÍREZ-FLORES,¹ AND R. E. BALDERAS-NAVARRO^{1,5}

¹Instituto de Investigación en Comunicación Óptica (IICO-UASLP), Av. Karakorum 1470, Lomas 4ta. Secc., San Luis Potosí C.P. 78210, Mexico

²Unidad Académica de Ingeniería Eléctrica, Benemerita Universidad Autónoma de Zacatecas, Jardín Juárez 147, Zona Centro, Zacatecas, C.P. 98000, Mexico

³GROC-UJI, Institute of New Imaging Technologies (INIT), Universitat Jaume I, Avda. Sos Baynat s/n, 12071 Castelló, Spain

⁴e-mail: a253595@alumnos.uaslp.mx

⁵e-mail: raul.balderas@uaslp.mx

*Corresponding author: arazama@auz.edu.mx

Received 14 April 2021; revised 23 June 2021; accepted 3 July 2021; posted 6 July 2021 (Doc. ID 427698); published 0 MONTH 0000

Hadamard, cosine, and noiselet bases are implemented into a digital holographic microscope based on single-pixel imaging with the capability to retrieve images of complex objects. The object is illuminated with coherent light modulated with different patterns deployed in a digital micromirror device, and the resulting fields are captured by single-pixel detection. For amplitude images, the experimental results of the three bases are evaluated with the peak SNR criteria. It is shown that the cosine basis recovers amplitude distributions with the best quality. Regarding phase images, the recovered ones compare well with those obtained with a CMOS camera. © 2021 Optical Society of America

<https://doi.org/10.1364/AO.427698>

1. INTRODUCTION

Digital holography (DH) has opened the door for many applications, such as phase microscopy for biomedical imaging and optical metrology [1–11]. However, the cost of conventional cameras depends on the operating wavelength, increasing the costs for nonvisible wavelengths. An alternative is to use a single-pixel (SP) scheme, which uses a nonspatial resolution image sensor for registration, providing a low-cost imaging technique that can work in a wide spectral band [12–17]. In addition, it has been shown that SP cameras can work in low-light environments [5,18–20]. Jointly used with compressive sensing (CS), it is possible to decrease the number of measurements and the imaging recording time [14,15,18,21–23].

Several techniques based on single-pixel image (SPI) are being developed for different applications, such as microscopy [12,19,21,24,25], edge detection [26], imaging through dispersive media [5,18,27,28], computational color imaging [14,24,29], computational ghost imaging [30], and other applications [31,32]. In particular, SPI techniques have been applied to phase and complex amplitude imaging using both non-interferometric and interferometric approaches. Regarding

non-interferometric techniques, there are methods based on coherent diffraction [33], wavefront sampling with position sensing detectors [6], the transport of intensity equation [34], or reference-free holography [35]. Concerning interferometric approaches, in general all the methods are based on optical interferometers combining spatial light modulator (SLM) sampling of the complex pattern to be reconstructed with single-pixel detection. Among the different optical architectures, we can distinguish ghost imaging [22], Mach–Zehnder interferometers [28], Michelson interferometers with phase-encoded reference beams [36,37], or common path interferometers [37].

The SPI technique consists of the projection of a series of microstructured light patterns onto a sample, while a photodetector without spatial resolution records the light intensity associated with each pattern. In general, the object is sampled with functions comprising an orthogonal basis codified on a SLM. Based on the measurements and using a computational algorithm, the final image is reconstructed numerically. The approach based on Hadamard single-pixel imaging (HSI) calls for a deterministic model using functions of the Hadamard basis for sample illumination [6,12,18,19,21,22,27,28,36,38,39].



Frontiers

Dynamic behavior in a pair of Lorenz systems interacting via positive-negative coupling

L.J. Ontañón-García^a, I. Campos Cantón^b, J. Pena Ramirez^{c,*}^a *Coordinación Académica Región Altiplano Oeste, Universidad Autónoma de San Luis Potosí, Km 1 Carretera a Santo Domingo, Salinas de Hidalgo, 78600, San Luis Potosí, México*^b *Facultad de Ciencias, Universidad Autónoma de San Luis Potosí, Av. Parque Chapultepec 1570, San Luis 78210, S.L.P, México*^c *Applied Physics Division, CICESE Carretera Ensenada-Tijuana 3918, Zona Playitas, Ensenada, C.P. 22860, B.C. México*

ARTICLE INFO

Article history:

Received 18 July 2020

Revised 4 February 2021

Accepted 22 February 2021

Keywords:

Synchronization

Positive-negative coupling

Emergent behavior

ABSTRACT

A standard assumption when analyzing bidirectionally coupled systems is to consider that the coupling consists of a negative feedback interconnection and also, it is generally assumed that the coupling is symmetric. Here, we investigate, by means of an example, the limit behavior in a pair of bidirectionally coupled systems where the coupling structure is non symmetric and composed by a combination of *positive* and *negative* feedback. The example at hand is the well-know Lorenz system. It is demonstrated that, besides synchronization, the coupled systems exhibit emergent behavior characterized by a transition from a synchronized chaotic state to unsynchronized periodic behavior, i.e., each system converges to a different limit cycle. Furthermore, it is shown that the coupling strength and the initial conditions of the systems play a key role in the onset of bistability of solutions. For the analysis, we use the master stability function, the Euclidean distance between trajectories, bifurcation diagrams, and Lyapunov exponents. Additionally, the obtained results are experimentally validated using electronic circuits.

© 2021 Elsevier Ltd. All rights reserved.

1. Introduction

Coupled systems are ubiquitous in the real world. For example, pancreatic islets are composed by coupled cells, the generators in a power grid are coupled via transmission lines, and the transmitters and receivers in a communication system are coupled in order to interchange information. A key element—perhaps the most important—determining the limit behavior in coupled dynamical systems is the coupling, i.e., the medium or canal through which the systems interchange information/energy. Basically, the coupling can be either unidirectional or bidirectional [1]. For the latter case, the interaction is mutual such that the interconnected systems influence each other. For example, in the brain, the astrocytes and neurons are bidirectionally coupled [2] and also, the neuronal and the neurotransmission systems are mutually coupled, as recently shown in [3]. On the other hand, bidirectional couplings find applications in laser optics [4] and chemical reactions [5], just to mention a few. This type of interconnection is commonly represented by a negative feedback (see [6–9] and the references therein), in order to have stability of the closed-loop system. Furthermore,

when the interconnection is bidirectional, a group of coupled oscillators may also exhibit emergent behavior, i.e., behavior that arises as a consequence of the interconnection and that cannot be observed when the systems are uncoupled, see e.g. [10,11]. For instance, a group of bidirectionally coupled phase oscillators may exhibit a behavior called chimera, in which some of the oscillators show phase synchronization, whereas some of them remain unsynchronized [12,13]. Likewise, coupled oscillators may exhibit oscillation quenching [14], either in the form of amplitude death [15,16] or oscillation death [17].

For the particular case of bidirectionally coupled Lorenz systems, there exists a vast and mature literature. For example, in [18] and the references there in, it has been shown that a pair of bidirectionally coupled Lorenz systems can exhibit complete synchronization. Moreover, other types of synchronization can be observed, like for example, anti-phase synchronization [19], synchronization [20], generalized synchronization [22], robust synchronization [23], among others. On the other hand, for the case of an ensemble of Lorenz oscillators, partial synchronization, intermittency, or chimera states, among others, may appear [21,24,25].

Interestingly, a pair of Lorenz oscillators diffusively coupled may also exhibit a blowout bifurcation at certain critical value of coupling strength [26–28]. Below the critical value of coupling, the systems may exhibit either transient on-off intermit-

* Corresponding author.

E-mail addresses: luis.ontanon@uaslp.mx (L.J. Ontañón-García), icampos@ciencias.uaslp.mx (I. Campos Cantón), jpena@cicese.mx (J. Pena Ramirez).



Low concentration ($x < 0.01$) Gd doping of CeO₂ thin films for n-type layers deposited by spin coating

J.G.R. Hernández-Arteaga, H. Moreno-García, A.G. Rodríguez*

Coordinación para la Innovación y la Aplicación de la Ciencia y la Tecnología (CIACYT), Universidad Autónoma de San Luis Potosí (UASLP), Álvaro Obregón 64, San Luis Potosí, S.L.P. 78000, Mexico

ARTICLE INFO

Keywords:
Cerium oxide
Gadolinium
Doping
Diode

ABSTRACT

CeO₂ thin films with (x) Gd concentration $0.0006 < x < 0.4$ were synthesized by spin coating. At low Gd concentrations, $x < 0.01$, x-ray diffraction showed negligible variations in the lattice parameter and the material behaved as Gd doped CeO₂ with an electron concentration, measured by Hall effect, that varied from 6.5×10^{14} to $9.4 \times 10^{16} \text{ cm}^{-3}$. On the other hand, for $x > 0.01$, the lattice parameter increased in agreement to the addition of Gd atoms and the generation of oxygen vacancies. Raman spectroscopy showed that the main phonon shift had two contributions of opposite sign related to the changes in atomic bonding length and the presence of oxygen vacancies. Two p-n junctions were formed with a $x = 0.0025$ CeO₂:Gd layer and two different thin films as the p-type material, Sb₂S₃ and Si. Both heterostructures showed electronic diode behavior, confirming the doping of CeO₂ with Gd.

1. Introduction

Interest in Ceria (CeO₂) has grown in recent years due to the variety of applications based on this material. It has been shown that CeO₂ works as an electrolyte in solid oxide fuel cells (SOFC) with state of the art peak power density of 2 W/cm^2 at operating temperature from 600 to 650°C [1,2]. As a buffer layer, CeO₂ improves the conversion efficiency of Bi₂S₃/PbS solar cells from 0.14 to 1.27% [3]. In gas sensing, different sensitive elements based on CeO₂ have been used to detect CO₂, NO₂ and CO [4,5]. Rare earth (RE) doped CeO₂ solid solutions show catalytic activity in CO and C₆H₅CH₃ oxidation reactions [6,7]. The electrical conductivity of cerium dioxide is a crucial property in these applications. The compatibility of cerium dioxide with rare earth elements allows to improve the electrical properties of CeO₂ while retaining its fluorite crystalline structure even for RE concentrations as high as 55% [8,9]. The electrical conductivity in CeO₂ has two contributions, electronic and ionic. The first takes place by carrier transport and the second by the oxygen ions diffusing through vacancies sites [10]. The ionic conductivity in CeO₂ can be increased incorporating trivalent rare earth atoms such as Sm³⁺, Nd³⁺ and Gd³⁺. The concentration of these elements that produces a maximal value in ionic conductivity lies between 0.1 and 0.2 for each trivalent ion, depending on the synthesis method [11–13]. With the addition of Gd to CeO₂, the ionic conductivity takes

place in a temperature range between 400 and 700°C, in contrast to Y-stabilized zirconia, where the ionic conductivity occurs above 800°C, making CeO₂:Gd an excellent alternative as electrolyte in SOFC with lower operating temperature.

The more stable oxides of Gd and Ce are Gd₂O₃ and CeO₂, respectively. Thus, for every trivalent Gd that substitutes Ce, one oxygen vacancy appears to balance the electric charge and the ionic conductivity increases with oxygen vacancy density. Given the atomic radii of Gd (0.105 nm) and Ce (0.097 nm), the substitution of Ce with Gd atoms produces a lattice expansion. Recent results show that the limit concentration of Gd that can be incorporated in the lattice is between 0.5 and 0.6. As the lattice deforms and vacancy density increases with Gd concentration, the crystallite size decreases and the electron mobility is impaired. The electronic conductivity is usually neglected at high Gd concentrations, and detailed studies of the electronic properties are scarce [10]. In the literature, the main goal of Gd incorporation studies is to increase the ionic conductivity using concentrations between 0.1 and 0.2, the properties of CeO₂ doped with low Gd concentrations (< 0.1) have not been extensively studied. Electronic doping of CeO₂ would make it an excellent candidate for Si based electronics, given crystal structure and lattice parameter match to Si.

In this work, the structural and electrical properties of CeO₂ thin films with (x) Gd concentration $0.0006 < x < 0.4$ are studied. Gd is

* Corresponding author.

E-mail address: angel.rodriguez@uaslp.mx (A.G. Rodríguez).



Application of atomic force microscopy to assess erythrocytes morphology in early stages of diabetes. A pilot study

Alejandra Loyola-Leyva^a, Juan Pablo Loyola-Rodríguez^{b,*}, Yolanda Terán-Figueroa^c, Santiago Camacho-Lopez^d, Francisco Javier González^a, Simón Barquera^e

^a Coordination for Innovation and Application of Science and Technology (Coordinación para la Innovación y Aplicación de la Ciencia y Tecnología, CIACyT), Avenida Sierra Leona 550, Lomas 2^a sección, 78210, San Luis Potosí, S.L.P., Mexico

^b Faculty of Dentistry, Popular Autonomous University of the State of Puebla, 21 sur 1103, Barrio de Santiago, 72410, Puebla, Puebla, Mexico

^c Faculty of Nursing and Nutrition, Autonomous University of San Luis Potosí (Universidad Autónoma de San Luis Potosí), Lateral Av. Salvador Nava, Lomas, 78290, San Luis Potosí, S.L.P., Mexico

^d Department of Optics, Center for Scientific Research and Higher Education of Ensenada (Centro de Investigación Científica y de Educación Superior de Ensenada, CICESE), Carretera Ensenada-Tijuana 3918. Zona Playitas, Ensenada, Baja California, Mexico

^e Center for Nutrition and Health Research. National Institute of Public Health. Address: Av. Universidad No.655 Col Sta. Ma. Ahuacatlán. Cuernavaca, Morelos, Mexico

ARTICLE INFO

Keywords:

Atomic force microscopy
Erythrocytes
Morphology
Prediabetes
Metabolic syndrome
Type 2 diabetes mellitus

ABSTRACT

The study aim was to assess the application of atomic force microscopy (AFM) to evaluate erythrocyte morphology in early stages of type 2 diabetes mellitus, and the association with biochemical, anthropometric, diet, and physical activity indicators.

This was a pilot cross-sectional study with four groups: healthy individuals, people with prediabetes (PDG), metabolic syndrome (MSG), and diabetes mellitus group (DMG). Blood samples were obtained to assess the erythrocyte morphology and biochemical parameters. Anthropometrical measurements were taken. Besides, a diet and a physical activity questionnaire were applied.

The evaluation of the erythrocyte morphology through the AFM showed quantitative and qualitative alterations in the cell's form and size. Compared to the healthy group, the PDG had a reduction in height ($-0.80 \mu\text{m}$, $p < 0.05$), and an increase in axial ratio ($-0.09 \mu\text{m}$, $p < 0.05$); the MSG had lower concave depth ($-0.19 \mu\text{m}$, $p < 0.05$); and the DMG had a decreased height ($-0.46 \mu\text{m}$, $p < 0.05$) and concave depth ($-0.29 \mu\text{m}$, $p < 0.05$), and higher axial ratio ($+0.08 \mu\text{m}$) and thickness ($+0.32 \mu\text{m}$, $p < 0.05$). The PDG vs. DMG had a statistically significant difference in concave depth ($+0.23 \mu\text{m}$, $p < 0.05$) and thickness ($-0.26 \mu\text{m}$, $p < 0.05$). The MSG was different than the DMG in variables like axial ratio ($-0.05 \mu\text{m}$) and thickness ($-0.25 \mu\text{m}$). Besides, higher values of age, HbA1c, triglycerides, body mass index, waist-to-hip ratio, and physical inactivity were associated with altered erythrocyte morphology.

AFM is a promising instrument to assess early but subtle changes in erythrocyte morphology (height, axial ratio, concave depth, thickness) before significant pathological conditions, such as type 2 diabetes mellitus. HbA1c might have a major effect in altered morphology, vs. metabolic parameters like high triglycerides, body mass index, waist, and physical inactivity.

1. Introduction

Type 2 diabetes mellitus (T2DM) is a significant public health problem because it is the major cause of blindness, kidney failure, heart attacks, stroke and lower limb amputation. Its prevalence has been

rising more rapidly in low and middle income countries (World Health Organization, 2020). In 2017, Mexico was sixth globally, with the highest prevalence of T2DM (12 million, CI 6–14.3 million). According to the Mexican National Health and Nutrition Survey 2018, the prevalence of T2DM (people with previous diagnosis) was 10.3 % (8.6 million

* Corresponding author.

E-mail addresses: aleloleyva@yahoo.com.mx (A. Loyola-Leyva), juanpablo.loyola8@gmail.com (J.P. Loyola-Rodríguez), yolandt@uaslp.mx (Y. Terán-Figueroa), camachol@cicese.mx (S. Camacho-Lopez), javier.gonzalez@uaslp.mx (F.J. González), sbarquera@insp.mx (S. Barquera).

<https://doi.org/10.1016/j.micron.2020.102982>

Received 24 July 2020; Received in revised form 4 November 2020; Accepted 5 November 2020

Available online 7 November 2020

0968-4328/© 2020 Elsevier Ltd. All rights reserved.



Comment on “Evaluating the efficiency of infrared breast thermography for early breast cancer risk prediction in asymptomatic population”

Throughout the years, several publications have suggested that Infrared breast thermography (IBT) is a tool with the potential for early breast cancer detection [1–4]. In particular, evaluating its efficiency on the asymptomatic population would be of interest. We read with great interest the paper by Gogoi et al. titled “Evaluating the Efficiency of Infrared Breast Thermography for Early Breast Cancer Risk Prediction in Asymptomatic Population” [5], where IBT is reported as a potential technique for early detection of breast pathologies, stating that “the mean [bilateral difference of] temperature is statistically significant in separating healthy thermograms from the benign ones”. From careful analysis of the work presented by Gogoi et al. it is our opinion that an incorrect statistical method was used to find whether those differences were significant or not which compromises the main conclusions presented in this work.

The authors tried to compare the statistical means among three samples (Healthy, Benign and Malignant) and do so under the assumption that the underlying distribution is not normal. In these situations, a nonparametric alternative to the one-way ANOVA must be used [6,7]. More specifically the Kruskal-Wallis test should be applied, not the Wilcoxon test [6,7], which was the test used in Gogoi et al. [5]. In fact, the Kruskal-Wallis test is a generalization of the Wilcoxon test to enable comparison of more than two groups [7,8]. However, using only the Kruskal-Wallis test allows for testing whether samples come from the same distribution [9]. If we want to determine which pairs of groups are different (healthy vs. benign, healthy vs. malignant, benign vs. malignant) a post-hoc procedure must be performed [9,10], such as the Dunn correction [7] or even a more conservative correction, such as Bonferroni's [11].

The Wilcoxon test (also known as the Wilcoxon-Mann-Whitney rank-sum test) and the Kruskal-Wallis test are equivalent when there are only two groups of patients [12]. Using pairwise Wilcoxon tests in this dataset is not recommended, because they do not retain information from the complete data set, by not using the pooled variance of all the observations applied in the Kruskal-Wallis test [7].

By using the temperature values manually obtained from Fig. 3 of Gogoi et al. the statistical analysis with post-hoc corrections was

performed. The extracted values are displayed in Fig. 1 for comparison to the original Fig. 3 from Gogoi et al.

Table 1 shows the data presented by Gogoi et al. but analyzed using the Dunn-Sidak or Bonferroni procedure and the p-values are compared to the Wilcoxon's test.

Even though the p-values shown in the first column of Table 1 are not exactly the same as those obtained by Gogoi et al. [5] due to the unavailability of the original data; the results corrected for multiple comparisons do not support the following statements on page 206: (1) “the mean temperature is statistically significant in separating healthy thermograms from the benign ones” and (2) “mean and mode temperatures are statistically significant in separating the benign thermograms from the malignant ones”.

It is our opinion that digital infrared thermography can be a valuable adjunct tool in breast cancer screening due to its high sensitivity [13–15], however the distinction between benign and malignant breast pathology has proved to be a challenging problem. In order to evaluate the screening effectiveness of digital breast thermography, patients with anomalous temperature patterns were gathered into a single group (benign + malignant $n = 35$) and compared to healthy controls ($n = 25$), using the Wilcoxon test (Table 2). Our analysis shows a significant difference between the groups for all features, except the bilateral maximum temperature difference, implying that it is possible to discern healthy patients from those with anomalous temperature patterns, either benign or malignant. These findings are aligned with previous research [16] performed on publicly available data [17] and support the use of infrared breast thermography as an adjunct tool in screening.

Declaration of Competing Interest

The authors declare that they have no known competing financial interests or personal relationships that could have appeared to influence the work reported in this paper.

Thermal Simulations of Cancerous Breast Tumors and Cysts on a Realistic Female Torso

Francisco Javier González

Universidad Autónoma de San Luis Potosí,
San Luis Potosí 78000, Mexico;
HIGIA Inc.,
Diagonal Patriotismo 12,
Col. Hipódromo Condesa,
CDMX 06100, Mexico
e-mail: javier.gonzalez@uaslp.mx

Medical thermography has been around for several decades however due to its low specificity it has not become a popular medical diagnostic technique. The development of computational models of heat transfer in biological tissue can provide a deeper knowledge of healthy and nonhealthy thermal patterns which could increase the specificity of this technique increasing its usefulness in clinical diagnosis. In this work, the thermal pattern of cancerous tumors and cysts are calculated through finite element computer simulations using a real human female torso. The simulation results show a thermal pattern that agrees with infrared thermal images taken from female subjects, the simulated thermal patterns show real thermal features that do not appear in simulations performed using other approximate geometries of the breast. Results show that the temperature on the region of the skin closest to the tumor decreases for cysts while it increases for malignant tumors. The temperature patterns show a 20% deviation from thermal simulations using a hemispherical model of the breast, these results reinforce the notion that the geometry used for thermal simulation plays an important role in the accuracy of the simulations. These results are a first step in understanding benign and malignant thermal processes of the breast which might help increase the usefulness of infrared imaging in breast clinical diagnosis. [DOI: 10.1115/1.4049957]

Keywords: breast thermography, breast cancer, finite element simulation, heat transfer

1 Introduction

Temperature changes in the body have been recognized as an indicator of illness for centuries, localized temperature variations due to inflammatory or ischemic events are common in a great variety of diseases [1], these changes are due to changes in blood perfusion which are responsible, along with the metabolic heat generation of tissue, for the local temperature of tissue and organs. In the case of cancerous breast tumors, there is an increase in vascularity due to angiogenesis and a higher metabolic heat rate generation compared to healthy tissue, this induces an increase in the local temperature of the tumor which generates an increase in the temperature of the surrounding skin, this increase in skin temperature can be detected with modern infrared imaging equipment [2].

Infrared imaging has been used to detect breast abnormalities since the 1950s [3], and was included as one of the breast cancer detection techniques in “The early Breast Cancer Detection and Demonstration Projects,” which were carried out between 1973 and 1981 by the American Cancer Society and National Cancer Institute of the United States [4]. After these studies the U.S. Food and Drug Administration (FDA) approved in 1982 infrared imaging as an adjunctive breast cancer screening procedure [4].

Even though approved by the FDA as an adjunctive breast cancer screening technique, the use of infrared imaging has not become mainstream due to its low specificity and due to the incorrect use and advertisement of thermography as a stand-alone technique for breast cancer screening and breast cancer detection. The FDA has issued several warnings to clinics and medical practitioners who claim thermography can be used instead of mammography or that thermography has a clinical advantage over mammography [5].

By developing more accurate computational models of heat transfer in biological tissue a better understanding of healthy and

nonhealthy thermal patterns can be obtained, this knowledge could improve the usefulness of infrared imaging as an adjunct tool in clinical diagnosis [4], it will also give a better understanding of the capabilities of thermography and how these functional images can be used in conjunction with anatomical images to increase the effectiveness of breast cancer screening and detection.

The most widely used physical model to simulate numerically heat transfer in biological tissue is the one developed by Pennes in 1948 [6], this model is still in use due to the convenience of not needing information on the discrete vasculature [7]. This model provides accurate approximations for tissues, such as the female breast, that have capillary vessels smaller than 300 μm [8].

The model introduced by Pennes describes the effects of metabolism and blood perfusion on the energy balance within the tissue, these two effects were incorporated into the standard thermal diffusion equation, resulting in the following bioheat equation:

$$\rho c \frac{\partial T}{\partial t} = \nabla \cdot k \nabla T + \rho_b c_b \omega_b (T_a - T) + q_{\text{met}} \quad (1)$$

where k is the thermal conductivity of tissue, ρ_b and c_b are the density and the specific heat of the blood, ω_b is the blood perfusion rate (ml/s/ml), q_{met} is the metabolic heat generation rate (W/m^3), T_a is the arterial blood temperature, and T is the local temperature of the breast tissue. The temperature of the arterial blood can be approximated as the core temperature of the body [4].

Thermal computer simulations of breast pathologies have been explored in the past using several different geometries, these include rectangular [8], spherical [9,10], and geometries deformed by gravity effects [11]. The temperature patterns resulting from these geometries do not agree completely with experimental observations [12]. Even though the thermal parameters in simulations reported in the literature have been similar, there is a clear difference in thermal patterns that arises from the simulation

Manuscript received October 13, 2019; final manuscript received January 6, 2021; published online March 9, 2021. Assoc. Editor: John LaDisa.

Thermal simulations of cancerous breast tumors and cysts on a realistic female torso

Francisco Javier González^{1,2}

¹Universidad Autónoma de San Luis Potosí, San Luis Potosí, 78000, México

²HIGIA Inc., Diagonal Patriotismo 12, Col. Hipódromo Condesa, CDMX, 06100, Mexico

javier.gonzalez@uaslp.mx

Keywords: Breast thermography, breast cancer, finite element simulation, heat transfer.

Abstract

Medical thermography has been around for several decades however due to its low specificity it has not become a popular medical diagnostic technique. The development of computational models of heat transfer in biological tissue can provide a deeper knowledge of healthy and non-healthy thermal patterns which could increase the specificity of this technique increasing its usefulness in clinical diagnosis. In this work the thermal pattern of cancerous tumors and cysts are calculated through finite element computer simulations using a realistic human female torso. The simulation results show a thermal pattern that agrees with infrared thermal images taken from female subjects, the simulated thermal patterns show real thermal features which do not appear in simulations performed using other approximate geometries of the breast. Results show that the temperature on the region of the skin closest to the tumor decreases for cysts while it increases for malignant tumors. The temperature patterns show a 20% deviation from thermal simulations using a hemispherical model of the breast, these results reinforce the notion that the geometry used for thermal simulation plays an important role in the accuracy of the simulations. These results are a first step in understanding benign and malignant thermal processes of the breast which might help increase the usefulness of infrared imaging in breast clinical diagnosis.

1. Introduction

Temperature changes in the body have been recognized as an indicator of illness for centuries, localized temperature variations due to inflammatory or ischemic events are common in a great variety of diseases [1], these changes are due to changes in blood perfusion which are responsible, along with the metabolic heat generation of tissue, for the local temperature of tissue and organs. In the case of cancerous breast tumors there is an increase in vascularity due to angiogenesis and a higher metabolic heat rate generation compared to healthy tissue, this induces an increase in the local temperature of the tumor which generates an increase in the temperature of the surrounding skin, this increase in skin temperature can be detected with modern infrared imaging equipment [2].

Infrared imaging has been used to detect breast abnormalities since the 1950's [3], and was included as one of the breast cancer detection techniques in "The early Breast Cancer Detection and Demonstration Projects," which were carried out between 1973 and 1981 by the American



Nucleation and diffusion processes during the stacking of bilayer quantum dot InAs/GaAs heterostructures

C.A. Mercado-Ornelas^a, L.I. Espinosa-Vega^a, I.E. Cortes-Mestizo^b, F.E. Perea-Parrales^a,
A. Belio-Manzano^a, V.H. Méndez-García^{a,*}

^a Center for the Innovation and Application of Science and Technology, Universidad Autónoma de San Luis Potosí (UASLP), Av. Sierra Leona #550, Col. Lomas 2a Sección, 78210 San Luis Potosí, Mexico

^b CONACYT-Center for the Innovation and Application of Science and Technology, Universidad Autónoma de San Luis Potosí (UASLP), Av. Sierra Leona #550, Col. Lomas 2a Sección, 78210 San Luis Potosí, Mexico

ARTICLE INFO

Communicated by Pierre Müller

Keywords:

InAs-quantum dots
Vertical stacking
Strain
Diffusion parameters
Critical thickness

ABSTRACT

The growth front stacking of bilayer quantum dot (BQD) InAs/GaAs heterostructures was studied by reflection high-energy electron diffraction (RHEED). The mean-field theory was employed to describe the quantum dots (QDs) nucleation, which was experimentally monitored during the intensity changes of the (002)-RHEED diffraction spot along the two- to three-dimensional (2D-3D) InAs growth mode transition. The diffusion parameter obtained from fits of the 2D-3D transition curves was associated to the rate of atoms supply from 2D and 3D islands precursors. The variation of the nucleation parameters during the vertical alignment of QDs associated to the coupling of strain fields were related to the changes of the QDs size and the wetting layer thickness. Numerical simulations indicated that these changes reduce the strain in the BQD heterostructures. Damped oscillatory behavior was observed for the InAs/GaAs critical thickness (H_c) as a function of the number of BQD. The bilayer number after which H_c did not vary significantly, coincided with the one without important variation of the diffusion parameters. The number of BQD layers required to reach this quasi-equilibrium condition depends on the growth parameters of the first layer and the spacer layer thickness, as supported by numerical simulations.

1. Introduction

Since the advent of the semiconductor nanotechnology, the self-assembly of quantum dots (QDs) in heteroepitaxial growth has acquired great importance in many fundamental research fields, such as nanoscience, solid-state physics, surface science, crystal growth, and low dimensional systems. In addition, due to the quantum confinement effects in them, these zero-dimensional nanostructures have huge potential for the development of next-generation nanodevices in technological fields such as optoelectronics, renewable energy, and data storage. InAs QD-based devices have been synthesized by molecular beam epitaxy (MBE), for example, mid- and far-infrared detectors, 4th generation solar cells, terahertz emitters, vertical-external-cavity surface-emitting lasers, and single-photon emitters [1–5]. These nanodevices are expected to present improved characteristics over those based on traditional materials, such as semiconductor quantum wells (QWs) [6]. However, the QDs structural parameters as their size, shape, and

chemical composition are not easily controlled during the epitaxial growth, and also these structural parameters determine the QDs' physical properties, which in turn influence the device performance. Moreover, for most of the applications of these zero-dimensional systems, the multiple QDs stacking is required, and therefore the geometry control becomes more challenging, since on every grown layer diffusion, segregation, alloying, ordering and strain effects are added to the already complex system. As part of the effort to gain control and reproducibility over QDs heterostructures, novel diagnostic and monitoring tools have been developed [7,8]. The availability of a real-time diagnosis tools that can directly be integrated with QDs manufacture would speed up developments and will significantly increase reliability and reproducibility issues. Reflection high-energy electron diffraction (RHEED) is a typical characterization technique that has been widely used to monitor the surface structure and morphology during the molecular beam epitaxial growth. RHEED has been employed with other analytical tools and assisted with theoretical models in order to get

* Corresponding author.






E-mail address: victor.mendez@uaslp.mx (V.H. Méndez-García).

<https://doi.org/10.1016/j.jcrysgro.2020.125959>

Received 10 July 2020; Received in revised form 30 October 2020; Accepted 16 November 2020

Available online 21 November 2020

0022-0248/© 2020 Elsevier B.V. All rights reserved.

Optical anisotropies of asymmetric double GaAs (001) quantum wellsO. Ruiz-Cigarrillo ^{*}, L. F. Lastras-Martínez,[†] E. A. Cerda-Méndez , G. Flores-Rangel ,
C. A. Bravo-Velazquez , R. E. Balderas-Navarro , and A. Lastras-Martínez*Instituto de Investigación en Comunicación Óptica, Universidad Autónoma de San Luis Potosí
Alvaro Obregón 64, 78000 San Luis Potosí, S.L.P., México*

N. A. Ulloa-Castillo

*Tecnológico de Monterrey, School of Engineering and Science, Av. Eugenio Garza Sada Sur 2501, Monterrey, Nuevo León 64849, México*K. Biermann and P. V. Santos[‡]*Paul-Drude-Institut für Festkörperelektronik, Leibniz-Institut im Forschungsverbund Berlin e.V, Hausvogteiplatz 5-7, 10117, Germany*

(Received 3 November 2020; revised 9 January 2021; accepted 11 January 2021; published 25 January 2021)

In the present work, we were able to identify and characterize a source of in-plane optical anisotropies (IOAs) occurring in asymmetric double quantum wells (DQWs), namely a reduction of the symmetry from D_{2d} to C_{2v} as imposed by asymmetry along the growth direction. We report on reflectance anisotropy spectroscopy (RAS) of double GaAs quantum well structures coupled by a thin (<2 nm) tunneling barrier. Two groups of DQW systems were studied: one where both QWs have the same thickness (symmetric DQW) and another where they have different thicknesses (asymmetric DQW). RAS measures the IOAs arising from the intermixing of the heavy and light holes in the valence band when the symmetry of the DQW system is lowered from D_{2d} to C_{2v} . If the DQW is symmetric, residual IOAs stem from the asymmetry of the QW interfaces, e.g., that associated with Ga segregation into the AlGaAs layer during the epitaxial growth process. In the case of an asymmetric DQW with QWs with different thicknesses, the AlGaAs layers (that are sources of anisotropies) are not distributed symmetrically at both sides of the tunneling barrier. Thus the system loses its inversion symmetry, yielding an increase in the RAS strength. The RAS line shapes were compared with reflectance spectra in order to assess the heavy- and light-hole mixing induced by the symmetry breakdown. The energies of the optical transitions were calculated by numerically solving the one-dimensional Schrödinger equation using a finite-difference method. Our results are useful for interpretation of the transitions occurring in both symmetric and asymmetric DQWs.

DOI: [10.1103/PhysRevB.103.035309](https://doi.org/10.1103/PhysRevB.103.035309)**I. INTRODUCTION**

Nanostructures based on double quantum wells (DQWs) constitute an excellent platform to study the interactions between confined energy levels, e.g., intra-QW transitions between electrons and holes belonging to the same QW (direct excitons and trions), and inter-QW transitions occurring for electrons and holes resident in different QWs (indirect excitons and indirect trions) [1]. The strength of the direct and indirect transitions can be modulated by the application of external perturbations, such as external electric fields. The electric field modifies the tunneling probability, leading to the appearance of spatially indirect inter-QW excitons [1–3] and intra-QW charged excitons (trions) [1]. Such complex band structures offer interesting optical phenomena that exhibit a polarization dependence. In-plane optical anisotropies (IOAs) of AlGaAs/GaAs-based heterostructure have been studied extensively in the past several years by means of reflectance anisotropy spectroscopy (RAS). In the case of single QWs, several sources of IOAs have been

investigated: (i) the absence of a fourfold rotational symmetry axis at the AlGaAs/GaAs interface [4,5], (ii) asymmetric quantum wells [6], (iii) nonuniform segregation of Ga atoms at AlGaAs/GaAs interfaces [5,7], (iv) application of an external stress [8,9], and (v) asymmetric barriers [10]. In general, the observed IOA strength depends on the QW thickness. For example, for strain-induced IOAs, the RAS response increases with the well thickness [8,9], whereas it decreases with the well thickness for the anisotropies induced exclusively by the interfaces [5,8,10].

In DQW-based systems, the relative thickness of the QWs plays an important role in the anisotropy strength; namely, if both QWs have the same thickness (symmetric DQW), the IOA arises from the contributions of the AlGaAs/GaAs(QW) and GaAs(QW)/AlGaAs interfaces, which, in general, are not equivalent. If the QW thicknesses are different (asymmetric DQW), the system loses its inversion symmetry as a whole along a plane perpendicular to the growth direction and passing through the center of the tunneling barrier; therefore, the interfaces of the DQW system are not distributed symmetrically at both sides of the tunneling barrier, leading to an increase of the IOA signal.

In this paper, we report on RAS experiments on DQWs coupled by a thin barrier (1.98 nm) and different relative thicknesses. We find that by increasing the thickness of one

^{*}oscarruiz@cactus.iico.uaslp.mx[†]lflm@cactus.iico.uaslp.mx[‡]santos@pdi-berlin.de



Multifractal analysis of the symmetry of a strictly isospectral energy landscape on a square lattice



J. de la Cruz^{a,*}, J.S. Murguía^b, H.C. Rosu^a

^aInstituto Potosino de Investigación Científica y Tecnológica, Camino a la Presa San José 2055, Lomas 4^a sección, 78216 San Luis Potosí, S.L.P., Mexico

^bFacultad de Ciencias, Universidad Autónoma de San Luis Potosí, Avenida Parque Chapultepec 1570, 78210 San Luis Potosí, S.L.P., Mexico

ARTICLE INFO

Article history:

Received 15 December 2020

Received in revised form 27 February 2021

Accepted 5 March 2021

Available online 17 March 2021

Keywords:

Multifractal

Hölder regularity

Isospectral

Symmetry

Riccati equation

ABSTRACT

We use the Hölder regularity analysis to study the symmetry breaking and recovery due to a parametric potential generated via the strictly isospectral factorization method. The initial potential is two-dimensional and periodic in the two Cartesian directions, with the symmetry group P_{4mm} . The resulting parametric isospectral potential display a P_m symmetry for values of the parameter moderately close to the singular value γ_s . However, at large values of the parameter, visually around $\gamma = \gamma_s + 110$, the original symmetry is recovered. For a much higher precision value of the parameter for this symmetry recovery, we show that the multifractal spectrum of the parametric potential can be conveniently used. In the latter case, we obtain $\gamma = \gamma_s + 201.085$ for three decimal digits precision.

© 2021 Elsevier B.V. All rights reserved.

1. Introduction

In 1984, Mielnik [1] obtained the parametric Darboux isospectral potential $V(x, \gamma) = x^2/2 - d/dx[\log(e^{-x^2/2} + \gamma)]$ for the case of the harmonic oscillator potential, $V_{\text{harm}} = x^2/2$, and since then many parametric isospectral potentials have been discussed in the literature [2]. Here, Mielnik's method is applied to a periodic two-dimensional potential with identical sinusoidal components on both Cartesian axes which is of interest in textures of energy landscapes. The main goal is to obtain a very precise value (much beyond the visual one) of the Darboux deformation parameter γ at which the symmetry associated to the original potential is recovered. The feature of symmetry recovery in this case is based on the well known fact that when $\gamma \rightarrow \infty$ the parametric deformation goes to zero. From the strict calculus point of view this comes out from the fact that in Eq. (6) below, γ stands in the denominator of ϕ and as such the ϕ term goes to zero at increasing γ . Physically, it is well known that γ is related to the change of boundary conditions from Dirichlet to Robin ones [3], and so the recovery of the initial symmetry can be controlled through external fields. We notice that the issue of (super) symmetry breaking and recovery has been discussed previously for relativistic quantum field models, but focused on the concept of mass generation, see e.g. [4,5], while in

condensed matter physics, the same issue has been related to phase transitions, either of equilibrium or non-equilibrium type.

The symmetry operations for the chosen periodic potential are $\pi/2$ rotations applied at the center of the cell and reflections over the axis and diagonals, while the deformed potential landscapes only possess a reflection with respect to the principal diagonal. When the deformation parameter takes a sufficiently high value the symmetry operations for the deformed potential are very close to the non deformed ones with a high level of precision and one can say that all the lost symmetries are recovered.

The effect of the deformation parameter is to modify the local maxima and minima distribution in the deformed potential, which physically implies that the probability density is redistributed over the landscape as a function of the deformation parameter, and becomes the same as that of the original potential when the deformation parameter is increased. In practice, the level of the achieved symmetry recovery is high already at moderate values of γ , but we are interested in much more precise values of this parameter such that the initial potential landscape and the corresponding deformed one can be considered as indistinguishable.

To find such precise values, we use the multifractal analysis which allows to study in detail the distribution of singularities of a function. The spectrum of singularities depends on the Hölder exponents that are used generically in the signal processing area since they allow the characterization of the local regularity of a signal or a function [6]. Moreover, our multifractal approach to isospectral potential energy landscapes and their symmetry recovery

* Corresponding author.



Multiscale energy profile of maximally nonlocal quantum CHSH scenarios

José Manuel Méndez Martínez*, J.S. Murguía

Laboratorio Nacional CI3M, Facultad de Ciencias, Universidad Autónoma de San Luis Potosí, Álvaro Obregón 64, C. P. 78000, San Luis Potosí, S.L.P., Mexico

ARTICLE INFO

Article history:

Received 12 November 2020
 Received in revised form 12 April 2021
 Accepted 15 April 2021
 Available online 20 April 2021
 Communicated by M.G.A. Paris

Keywords:

Quantum correlations
 Quantum CHSH scenarios
 Multiscale energy profiles
 Haar wavelets
 Quantum signals compression

ABSTRACT

The outcomes measured by Alice and Bob in quantum CHSH scenarios are collected as digital signals and decomposed into a set of trend and fluctuation subsignals. We show that the shortest scales subsignals contain the highest energy concentrations. Later, the subsignals' energy is characterized in terms of the entanglement degree. For maximally entangled qubits, the dominant energy in the signals measured locally by the observers is the fluctuation energy (ratios from 0.5 to 1), whereas in the signals considering the outputs of both parties is the trend energy (ratios from 0.5 to 0.75). The energy profile attained is a key step toward the compression of quantum signals via wavelet techniques.

© 2021 Elsevier B.V. All rights reserved.

1. Introduction

In the last years nonlocality has become a key information-processing resource. Applications in fields as cryptography [1–3], information processing [4,5] and communications [6] evince its power and usefulness. This usefulness can be extended to the area of signal processing and data transmission by considering quantum correlations as digital signals. One of the main matters of interest in signal processing is data compression, which involves the energy redistribution within a data sequence in order to identify and retain only the most significant components of it. Hence arises the question if quantum signals can be compressed without losing their entangled and nonlocal character. At least not completely.

A first step toward the compression of signals produced by pairs of entangled qubits is the determination of their energy profile. It is desirable that such a profile considers both the nonlocal component of the signals and the entanglement degree of the qubits. Of particular interest are the signals with a high nonlocal component, specially those producing the maximal violation of the CHSH inequality for a given state [7–10].

Among the tools used for energy compaction in digital signals stands out the wavelet analysis, which enables data processing at different resolutions or *scales* (the wavelet analog of wavelength) [11–13]. One of its major characteristics is its capacity to redistribute the energy of a digital signal and compact it into a smaller

subsignal, usually the trend subsignal (small fluctuation feature) [14]. This property has been exploited in the development of algorithms for image and audio compression [14], as well as in the implementation of cryptographic protocols [15,16].

So, with the aim of studying the feasibility of compressing quantum signals, in this paper we apply the wavelet analysis to the correlation signals generated by pairs of qubits in maximally nonlocal CHSH scenarios [10]. The energy profile of the signals is characterized in terms of both the scale of the component subsignals and the entanglement degree of the qubits generating the signals. Given that the outputs in the CHSH scenarios only may take two values, the Haar basis [17] has been chosen to carry out the analysis.

2. CHSH correlational scenarios

In the CHSH scenario [18,19,10], two distant parties (Alice and Bob) agree to share pairs of entangled qubits prepared in the state

$$|\psi\rangle = e^{i\alpha_1} \cos \beta |01\rangle + e^{i\alpha_2} \sin \beta |10\rangle, \quad (1)$$



with $\beta \in [0, \pi/2]$ and $\alpha_i \in [0, 2\pi]$. The content of entanglement in $|\psi\rangle$ is measured by its Wootters' concurrence, $W_\psi = \sin 2\beta$ [20, 21]. In the setup Alice and Bob play the role of party $i = 1$ and 2, respectively. Each party has access to a local binary input $x_i \in \{0, 1\}$ associated to the setup vectors \vec{a}_{x_1} for Alice and \vec{b}_{x_2} for Bob. These vectors allow the observers to carry out the local measurements $\mathbb{A}_{x_1} = \vec{\sigma} \cdot \vec{a}_{x_1}$ and $\mathbb{B}_{x_2} = \vec{\sigma} \cdot \vec{b}_{x_2}$, where $\vec{\sigma} = (\sigma_x, \sigma_y, \sigma_z)$ denotes the

* Corresponding author.

E-mail address: manuel.mendez@uaslp.mx (J.M. Méndez Martínez).

Article

Scaling Analysis of an Image Encryption Scheme Based on Chaotic Dynamical Systems

L. E. Reyes-López ¹ , J. S. Murguía ^{2,3,*} , H. González-Aguilar ^{2,3}, M. T. Ramírez-Torres ⁴, M. Mejía-Carlos ¹ and J. O. Armijo-Correa ²

¹ Instituto de Investigación en Comunicación Óptica, Universidad Autónoma de San Luis Potosí, Álvaro Obregón 64, 78000 San Luis Potosí, Mexico; lerl220591@gmail.com (L.E.R.-L.); marcela.mejia@uaslp.mx (M.M.-C.)

² Facultad de Ciencias, Universidad Autónoma de San Luis Potosí, Av. Chapultepec 1570, Priv. del Pedregal, 78295 San Luis Potosí, Mexico; herman@fc.uaslp.mx (H.G.-A.); omaramijo89@gmail.com (J.O.A.-C.)

³ Laboratorio Nacional CI3M, Facultad de Ciencias, Universidad Autónoma de San Luis Potosí, Av. Chapultepec 1570, Priv. del Pedregal, 78295 San Luis Potosí, Mexico

⁴ Coordinación Académica Región Altiplano Oeste, Universidad Autónoma de San Luis Potosí, Carretera Salinas-Santo Domingo 200 Salinas, 78600 San Luis Potosí, Mexico; tulio.torres@uaslp.mx

* Correspondence: ondeleto@uaslp.mx

Abstract: Despite that many image encryption systems based on chaotic or hyperchaotic systems have been proposed to protect different kinds of information, it has been crucial to achieve as much security as possible in such systems. In this sense, we numerically implement a known image encryption system with some variants, making special emphasis when two operations are considered in the scrambling stage. The variants of such an encryption system are based on some hyperchaotic systems, which generated some substitution boxes and the keys of the system. With the aim to have a more complete evaluation, some internal stages of the image encryption scheme have been evaluated by using common statistical tests, and also the scaling behavior of the encrypted images has been calculated by means of a two-dimensional detrended fluctuation analysis (2D-DFA). Our results show that the image encryption systems that include two operations or transformations in the scrambling stage present a better performance than those encryption systems that consider just one operation. In fact, the 2D-DFA approach was more sensitive than some common statistical tests to determine more clearly the impact of multiple operations in the scrambling process, confirming that this scaling method can be used as a perceptual security metric, and it may contribute to having better image encryption systems.

Keywords: image encryption system; S-box; two-dimensional multifractal detrended fluctuation analysis



Citation: Reyes-López, L.E.; Murguía, J.S.; González-Aguilar, H.; Ramírez-Torres, M.T.; Mejía-Carlos, M.; Armijo-Correa, J.O. Scaling Analysis of an Image Encryption Scheme Based on Chaotic Dynamical Systems. *Entropy* **2021**, *23*, 672. <https://doi.org/10.3390/e23060672>

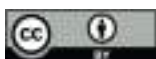
Academic Editor: Dimitri Volchenkov

Received: 15 April 2021

Accepted: 23 May 2021

Published: 27 May 2021

Publisher's Note: MDPI stays neutral with regard to jurisdictional claims in published maps and institutional affiliations.



Copyright: © 2021 by the authors. Licensee MDPI, Basel, Switzerland. This article is an open access article distributed under the terms and conditions of the Creative Commons Attribution (CC BY) license (<https://creativecommons.org/licenses/by/4.0/>).

1. Introduction

Nowadays, the way in which society communicates has radically changed with the fast development of computers and the internet. In particular, multimedia communication has been gaining momentum in the exchange of information at all social levels. Therefore, in recent years, security and confidentiality have been of considerable interest. Text encryption has been found to be very different from image encryption due to some inherent image characteristics, such as data-rich capacity, high redundancy, and high correlation between adjacent pixels. Due to the demand to have a secure transmission through any means of communication, a great variety of encryption systems has been proposed [1–5].

Chaos theory is used in many fields of science due to its special properties, and cryptography is no exception. Many visual data encryption systems based on chaos theory consider the principle of applying chaotic maps to obtain highly mixing properties, which are similar to cryptographic systems. Encryption systems that involve chaotic systems

An elementary approach to subdiffusion

Elena Floriani

*Aix Marseille Univ, Université de Toulon,
CNRS, CPT, Marseille, France
floriani@cpt.univ-mrs.fr*

Ricardo Lima

*Dream and Science Factory, Marseille, France
dream.and.science@gmail.com*

Edgardo Ugalde*

*Instituto de Física,
Universidad Autónoma de San Luis Potosí, México
ugalde@ifisica.uaslp.mx*

Received 2 August 2020

Revised 8 November 2020

Accepted 22 December 2020

Published 3 March 2021

We consider a basic one-dimensional model which allows to obtain a diversity of diffusive regimes whose speed depends on the moments of a per-site trapping time. This models a discrete subordinated random walk, closely related to the continuous time random walks widely studied in the literature. The model we consider lends itself to a detailed elementary treatment, based on the study of recurrence relation for the time- t dispersion of the process, making it possible to study deviations from normality due to finite time effects.

Keywords: Subordinated random walks; subdiffusion; recurrence relations; finite-time effects.

1. Introduction

The random walks with trapping times we study in this paper can be seen as the natural discrete version of the continuous time random walk (CTRW), which has been treated in mathematical physics literature since its introduction by Montroll and Weiss in 1965 [13]. A recent account on the subject can be found in [11], where CTRWs are considered as models for anomalous diffusion. A presentation of the

*Corresponding author.



Optical contrast in the near-field limit for structural characterization of graphene nanoribbons



G. Flores-Rangel^{a,*}, L.F. Lastras-Martínez^{a,*}, R. Castro-García^a, O. Ruiz-Cigarrillo^a, R.E. Balderas-Navarro^a, L.D. Espinosa-Cuellar^a, A. Lastras-Martínez^a, J.M.J. Lopes^b

^a Instituto de Investigación en Comunicación Óptica, Universidad Autónoma de San Luis Potosí Alvaro Obregón 64, 78000 San Luis Potosí, S.L.P., Mexico

^b Paul-Drude-Institut für Festkörperelektronik, Leibniz-Institut im Forschungsverbund Berlin e.V., Hausvogteiplatz 5-7, 10117 Berlin, Germany

ARTICLE INFO

Keywords:

Near-field scanning microscopy
Optical contrast
Graphene nanoribbons
Optical properties

ABSTRACT

Graphene nanoribbons (GNRs) are unique structures with interesting optical and electronic properties which have great potential of application in fields such as optoelectronics and nanoelectronics. Synthesis and characterization techniques of GNRs are quite important for the development of such technologies. In the case of the structural characterization, it is essential to develop quick and non-destructive approaches in order to determine properties such as thickness and uniformity of GNRs. In the present work we report the structural characterization of GNRs grown on stepped SiC (0001) surfaces by using a differential reflectance contrast (DRC) technique based on a near-field scanning optical microscope (NSOM). With this approach, it is possible to assess GNRs widths with dimension as small as 60 nm with a thickness of one or two graphene monolayers. Our results show that the DRC technique is powerful to analyze the morphology of GNRs grown on SiC (0001) substrates which is a promising wafer-scale platform for the development of graphene-based nanoelectronics.

1. Introduction

Graphene possesses unique properties with great potential applications in electronics and optics. In the last years a great effort has been done to characterize its mechanical [1], electrical [2] and optical properties [3,4]. Concerning nanoelectronic applications, graphene has several advantages: it is patternable, scalable and exhibits a very high mobility [5,6]. However, due to its gapless behavior graphene cannot be used in some applications like digital electronics. In this regard, different efforts have been directed toward opening a band gap in graphene without significantly affecting its mobility. Among them, we can mention applied uniaxial strain [7], chemical modifications (i.e. oxidation) and taking advantage of confinement effects. In the last case, graphene can be epitaxially grown on SiC to form ribbons (GNRs) with widths controlled by the growth conditions and the post growth annealing procedures [6,8,9]. The band gap of the GNRs is a function of the ribbon width [6]. Thus, controlled growth followed by reliable determination of properties such as width and thickness is of fundamental importance to tailor the properties of such nanostructures towards specific applications.

Optical techniques like Raman spectroscopy, have been successfully used as quick and non-destructive methods to determine the thickness

of graphene on different substrates [10]. However, a complication arises in the case of GNRs because the optical probe in such systems (due to the diffraction limit), is typically of 0.5 or 1 micrometers in diameter, making impossible to resolve individual GNRs that have widths of tens of nanometers. Thus, in this case only average optical response can be obtained. Another optical technique used to study the average response of GNRs systems, is the Reflectance Difference Spectroscopy/Reflectance Anisotropy Spectroscopy (RDS/RAS). This technique takes into account the high asymmetry (difference in the signal obtained in perpendicular crystallographic directions) of the GNRs. In particular we can mention, *in situ* RAS of GNRs grown on Au(788) [11], *ex situ* RAS of GNRs grown on stepped SiC (0001) [12] and recently the optical imaging and absorption spectroscopy of GNRs on insulating substrates [13].

To overcome the disadvantage that the diffraction limit has in the resolution of the optical measurements, recently, a near field optical microscopy (NSOM)-based methodology has been employed to analyze graphene layers exfoliated on SiO₂/Si substrates [4] and GNRs grown on SiC (0001) [12], with a lateral resolution of ~ 40 nm. In the case of graphene layers exfoliated on SiO₂/Si substrates, an NSOM-based difference reflectance contrast technique (DRC) has been used to map the thickness of the graphene across the surface [4]. DRC is based in the

* Corresponding author.

E-mail addresses: gflores@cactus.iico.uaslp.mx (G. Flores-Rangel), lflm@cactus.iico.uaslp.mx (L.F. Lastras-Martínez).

<https://doi.org/10.1016/j.apsusc.2020.147710>

Received 12 May 2020; Received in revised form 13 August 2020; Accepted 27 August 2020

Available online 10 September 2020

0169-4332/ © 2020 Elsevier B.V. All rights reserved.



UNIVERSITARIOS POTOSINOS

REVISTA DE DIVULGACIÓN CIENTÍFICA

Protagonista
de la endodancia

**DANIEL
SILVA-HERZOG
FLORES**

**LA CONTAMINACIÓN
DEL AIRE: UN
PROBLEMA DE
SALUD PÚBLICA**

**DIVULGACIÓN DE
LA HISTORIA
CON MEMES:
EL 12 DE OCTUBRE**



**Trastorno del sueño,
un problema de**

peso



9 77 1870 169005

LATINDEX: 24292

Roadmap

Roadmap on emerging hardware and technology for machine learning

Karl Berggren^{1,36} , Qiangfei Xia^{2,36} , Konstantin K Likharev³, Dmitri B Strukov⁴, Hao Jiang⁵, Thomas Mikolajick⁶ , Damien Querlioz⁷, Martin Salinga⁸ , John R Erickson⁹, Shuang Pi¹⁰, Feng Xiong⁹, Peng Lin¹, Can Li¹¹ , Yu Chen¹², Shisheng Xiong¹², Brian D Hoskins¹³, Matthew W Daniels¹³ , Advait Madhavan^{13,14}, James A Liddle¹³, Jabez J McClelland¹³, Yuchao Yang¹⁵ , Jennifer Rupp^{16,17}, Stephen S Nonnenmann¹⁸, Kwang-Ting Cheng¹⁹ , Nanbo Gong²⁰ , Miguel Angel Lastras-Montano²¹, A Alec Talin²², Alberto Salleo²³, Bhavin J Shastri²⁴ , Thomas Ferreira de Lima²⁵, Paul Prucnal²⁵, Alexander N Tait²⁶, Yichen Shen²⁷, Huaiyu Meng²⁷, Charles Roques-Carmes¹, Zengguang Cheng^{28,29} , Harish Bhaskaran²⁸, Deep Jariwala³⁰ , Han Wang³¹, Jeffrey M Shainline²⁶ , Kenneth Segall³², J Joshua Yang^{2,37} , Kaushik Roy³³, Suman Datta³⁴ and Arijit Raychowdhury³⁵

¹ Research Laboratory of Electronics, Massachusetts Institute of Technology, Cambridge, MA 02139, United States of America

² Department of Electrical and Computer Engineering, University of Massachusetts, Amherst, MA, United States of America

³ Stony Brook University, Stony Brook, NY 11794, United States

⁴ Department of Electrical and Computer Engineering, University of California at Santa Barbara, Santa Barbara, CA 93106, United States of America

⁵ School of Engineering & Applied Science Yale University, CT, United States of America

⁶ NaMLab gGmbH and TU Dresden, Germany

⁷ Université Paris-Saclay, CNRS, France

⁸ Institut für Materialphysik, Westfälische Wilhelms-Universität Münster, Germany

⁹ Department of Electrical and Computer Engineering, University of Pittsburgh, Pittsburgh, PA 15261, United States of America

¹⁰ Lam Research, Fremont, CA, United States of America

¹¹ Department of Electrical and Electronic Engineering, The University of Hong Kong, Hong Kong SAR, China

¹² School of information science and technology, Fudan University, Shanghai, People's Republic of China

¹³ Physical Measurements Laboratory, National Institute of Standards and Technology, Gaithersburg, MD 20899, United States of America

¹⁴ Institute for Research in Electronics and Applied Physics, University of Maryland, College Park, MD, United States of America

¹⁵ School of Electronics Engineering and Computer Science, Peking University, Beijing, People's Republic of China

¹⁶ Department of Materials Science and Engineering and Department of Electrical Engineering & Computer Science, Massachusetts Institute of Technology, Cambridge, MA 02139, United States of America

¹⁷ Electrochemical Materials, ETHZ Department of Materials, Hönggerberggring 64, Zürich 8093, Switzerland



Original content from this work may be used under the terms of the [Creative Commons Attribution 4.0 licence](https://creativecommons.org/licenses/by/4.0/). Any further distribution of this work must maintain attribution to the author(s) and the title of the work, journal citation and DOI.



Diagnostic accuracy of infrared thermal imaging for detecting COVID-19 infection in minimally symptomatic patients

Mario A. Martinez-Jimenez^{1,2,3} | Victor M. Loza-Gonzalez² |
E. Samuel Kolosovas-Machuca^{2,3,4} | Mercedes E. Yanes-Lane⁵ |
Ana Sofia Ramirez-GarciaLuna⁶ | Jose L. Ramirez-GarciaLuna^{2,7}

¹Emergency Department, Hospital Central “Dr. Ignacio Morones Prieto”, San Luis Potosi, Mexico

²Gabinete de Termografía Potosino, San Luis Potosi, Mexico

³Doctorado Institucional en Ingeniería y Ciencia de Materiales (DICIM-UASLP), Universidad Autónoma San Luis Potosi, San Luis Potosi, Mexico

⁴Coordinación para la Innovación y Aplicación de la Ciencia y la Tecnología, Universidad Autónoma San Luis Potosi, San Luis Potosi, Mexico

⁵Department of Epidemiology, McGill University, Montreal, Canada

⁶Instituto Nacional de Enfermedades Respiratorias, Ciudad de Mexico, Mexico

⁷Division of Experimental Surgery, McGill University, Montreal, Canada

Correspondence

Jose L. Ramirez-GarciaLuna, Division of Experimental Surgery, McGill University, 1650 Cedar Ave., Suite C10-124, H3G 1A4 Montreal, QC, Canada.

Abstract

Introduction: Despite being widely used as a screening tool, a rigorous scientific evaluation of infrared thermography for the diagnosis of minimally symptomatic patients suspected of having COVID-19 infection has not been performed.

Methods: A consecutive sample of 60 adult individuals with a history of close contact with COVID-19 infected individuals and mild respiratory symptoms for less than 7 days and 20 confirmed COVID-19 negative healthy volunteers were enrolled in the study. Infrared thermograms of the face were obtained with a mobile camera, and RT-PCR was used as the reference standard test to diagnose COVID-19 infection. Temperature values and distribution of the face of healthy volunteers and patients with and without COVID-19 infection were then compared.

Results: Thirty-four patients had an RT-PCR confirmed diagnosis of COVID-19 and 26 had negative test results. The temperature asymmetry between the lacrimal caruncles and the forehead was significantly higher in COVID-19 positive individuals. Through a random forest analysis, a cut-off value of 0.55°C was found to discriminate with an 82% accuracy between patients with and without COVID-19 confirmed infection.

Conclusions: Among adults with a history of COVID-19 exposure and mild respiratory symptoms, a temperature asymmetry of $\geq 0.55^\circ\text{C}$ between the lacrimal caruncle and the forehead is highly suggestive of COVID-19 infection. This finding questions the widespread use of the measurement of absolute temperature values of the forehead as a COVID-19 screening tool.

KEYWORDS

COVID-19, diagnosis, machine learning, screening, thermography

Martinez-Jimenez and Loza-Gonzalez authors contributed equally to this study.

Research Article

Determination of the Immunoglobulin G Spectrum by Surface-Enhanced Raman Spectroscopy Using Quasispherical Gold Nanoparticles

Alejandra Ortiz-Dosal ¹, Elizabeth Loredo-García,² Ana Gabriela Álvarez-Contreras,² Juan Manuel Núñez-Leyva,^{1,2} Luis Carlos Ortiz-Dosal,³ and Eleazar Samuel Kolosovas-Machuca ^{1,2}

¹Doctorado Institucional en Ingeniería y Ciencia de Materiales (DICIM-UASLP), Universidad Autónoma de San Luis Potosí, 550 Sierra Leona Ave., 78210 San Luis Potosí, SLP, Mexico

²Coordinación para la Innovación y Aplicación de la Ciencia y la Tecnología, Universidad Autónoma de San Luis Potosí, 550 Sierra Leona Ave., 78210 San Luis Potosí, SLP, Mexico

³Maestría en Ciencia e Ingeniería de los Materiales (MCIM-UAZ), Universidad Autónoma de Zacatecas, 801 López Velarde St., 9800 Zacatecas, Zac, Mexico

Correspondence should be addressed to Eleazar Samuel Kolosovas-Machuca; samuel.kolosovas@uaslp.mx

Received 19 September 2020; Revised 26 December 2020; Accepted 8 January 2021; Published 19 January 2021

Academic Editor: Sheng-Joue Young

Copyright © 2021 Alejandra Ortiz-Dosal et al. This is an open access article distributed under the Creative Commons Attribution License, which permits unrestricted use, distribution, and reproduction in any medium, provided the original work is properly cited.

Background. Immunoglobulins (Ig) are glycoprotein molecules produced by plasma cells in response to antigenic stimuli involved in various physiological and pathological conditions. Intravenous immunoglobulin (IVIG) is a compound whose composition corresponds to Ig concentrations in human plasma, predominantly IgG. It is used as a replacement treatment in immunodeficiencies and as an immunomodulator in inflammatory and autoimmune diseases. The determination of IgG concentrations is useful in the diagnosis of these immunodeficiencies. Surface-enhanced Raman spectroscopy (SERS) is a technique that allows protein quantification in a fast and straightforward way. **Objective.** This study is aimed at determining the Raman spectrum of IgG at physiological concentrations using quasispherical gold nanoparticles as a SERS substrate. **Methods.** We initially determined the Raman spectrum of IVIG at 5%. Subsequently, for SERS' characterization, decreasing dilutions of the protein were made by adding deionized water and an equal volume of the 5 nm gold quasispherical nanoparticle colloid. For each protein concentration, the Raman spectrum was determined using a 10x objective; we focused the 532 and 785 nm laser on the sample surface, in a range of 500-1800 cm^{-1} , with five acquisitions and an acquisition time of 30 seconds. **Results.** We obtained the IVIG spectrum using SERS up to a concentration of 75 mg/dl. The Raman bands correspond to aromatic amino acid side chains and the characteristic beta-sheet structure of IgG. **Conclusion.** The use of 5 nm quasispherical gold nanoparticles as a SERS substrate allows for detecting the Raman spectrum of IVIG at physiological concentrations.





1. Introduction

Immunoglobulins (Ig), also known as antibodies, are glycoprotein molecules produced by plasma cells in response to antigenic stimuli involved in various physiological and pathological conditions. The primary function of immunoglobulins corresponds to the adaptive immune response. They are subdivided, depending on the structure of the heavy

chains they contain, into several classes: IgM, IgG, IgD, IgA, and IgE. IgG is also subdivided into IgG1, IgG2, IgG3, IgG4 (decreasing order of abundance), and IgA in IgA1 and IgA2. IgG is the most abundant, with a plasma concentration of 700-1600 mg/dl, and constitutes 75 to 80% of all Ig. IgA corresponds to about 15%, with a plasma concentration of 70-400 mg/dl, while IgM's plasma concentration varies from 40 to 230 mg/dl. The determination of immunoglobulin



Deep convolutional neural networks for classifying breast cancer using infrared thermography

Juan Carlos Torres-Galván ^{a,b,c}, Edgar Guevara ^d, Eleazar Samuel Kolosovas-Machuca ^b, Antonio Ocegueda-Villanueva^e, Jorge L. Flores^f and Francisco Javier González ^a

^aTerahertz Science and Technology Center (C2T2) and Science and Technology National Lab (LANCyTT), Universidad Autónoma de San Luis Potosí, San Luis Potosí, Mexico; ^bFaculty of Science, Universidad Autónoma de San Luis Potosí, San Luis Potosí, México; ^cFaculty of Engineering, Universidad Autónoma de San Luis Potosí, San Luis Potosí, México; ^dCONACYT-Universidad Autónoma de San Luis Potosí, San Luis Potosí, Mexico; ^eSecretaría de Salud Jalisco, Instituto Jalisciense de Cancerología, Guadalajara, Mexico; ^fCUCEI, Universidad de Guadalajara, Guadalajara, Mexico

ABSTRACT

Infrared thermography is a technique that can detect anomalies in temperature patterns which can indicate some breast pathologies including breast cancer. One limitation of the method is the absence of standardised thermography interpretation procedures. Deep learning models have been used for pattern recognition and classification of objects and have been adopted as an adjunct methodology in medical imaging diagnosis. In this paper, the use of a deep convolutional neural network (CNN) with transfer learning is proposed to automatically classify thermograms into two classes (normal and abnormal). A population of 311 female subjects was considered analysing two approaches to test the CNN's performance: one with a balanced class distribution and the second study in a typical screening cohort, with a low prevalence of abnormal thermograms. Results showed that the transfer-learned ResNet-101 model had a sensitivity of 92.3% and a specificity of 53.8%, while with an unbalanced distribution the values were 84.6% and 65.3%, respectively. These results suggest that the model presented in this work can classify abnormal thermograms with high sensitivity which validates the use of infrared thermography as an adjunct method for breast cancer screening.

ARTICLE HISTORY


Received 12 January 2021
Accepted 12 April 2021

KEYWORDS

Deep convolutional neural networks; transfer learning; breast cancer screening; infrared thermography

Introduction

Breast cancer is the most common cancer in women worldwide and the third cause of death by malignant neoplasms in Mexican women [1,2]. The low survival rates can be explained mainly by the high proportion of women presenting with late-stage disease, if this disease is diagnosed in an early stage the survival rate is 90% [1]. The lack of access to health services in the country is one of the principal reasons that increment the mortality of this disease. Therefore, the use of techniques that help early detection could be a strategy to reduce the rate of deaths from breast cancer.

CONTACT Juan Carlos Torres-Galván  jctorres777@gmail.com  Terahertz Science and Technology Center (C2T2) and Science and Technology National Lab (LANCyTT), Universidad Autónoma de San Luis Potosí, Sierra Leona 550, Col. Lomas 2a. Sección, San Luis Potosí, SLP C.P. 78210, Mexico